Three-dimensional Variable Center of Mass Height Biped Walking Using a New Model and Nonlinear Model Predictive Control

Zhongqu Xie[a,b,c], Yulin Wang[a,*], Xiang Luo[b], Pierluigi Arpenti[c], Fabio Ruggiero[c], Bruno Siciliano[c]

[a]*Intelligent robotics lab, School of Mechanical Engineering, Nanjing University of Science and Technology, Xiaolingwei No.200 Xuanwu District, Nanjing, 210000, China.*
[b]*Bionic robotics lab, School of Mechanical Engineering, Southeast University, Dongnandaxue No.2 Jiangning District, Nanjing, 210000, China.*
[c]*PRISMA lab, Department of Electrical Engineering and Information Technology, University of Naples Federico II, Via Claudio 21, 80125, Naples, Italy.*

Abstract

This paper presents a trajectory generation algorithm for a three-dimensional (3D) biped robot that can adjust the center of mass (CoM) according to the environment. We adopt a new abstract model that supports vertical motion and rotation. Differing from traditional abstract models, the proposed full centroid dynamics inverted pendulum model fully considers the robot's movement and rotation. Unlike the zero moment point (ZMP), which only ensures the feet do not flip over, we also propose a new additional stability criterion, named zero frictional moment point (ZFMP), guaranteeing no yaw rotation while walking. Next, a nonlinear model predictive control is designed to generate the CoM trajectory, torso rotational angle, and adaptive footholds to induce various biped gaits. A full-dynamics 3D humanoid robot is simulated to test the proposed method while steering, walking underneath a low door, and walking with disturbances.

Keywords: 3D biped robot, full centroid dynamics inverted pendulum, nonlinear model prediction control, zero frictional moment point, variable CoM height.

1. Introduction

The control of a biped robot is challenging mainly due to its hard-to-stabilize dynamics. Compared to other mobile systems, e.g., wheeled or tracked robots, biped locomotion involves another complexity: the hybrid nature of stepping where the continuous model changes in each phase [1]. First, the fact that the biped robots can only have unilateral constraints with the environment leads to difficulty in balancing them [2]. Moreover, associated timing and the coordination control of redundant joints are other essential topics in controlling biped robots [3]. Beyond these, the robustness of biped locomotion is far achieved [4], leading to the fact that most of the existing robot biped walking is clunky and unnatural; thus, the main challenges are being human-like, energy-efficient, versatile, and of course, agile as humans [5, 6]. However, simplified models are widely used for computational convenience [1], resulting in unnatural center of mass (CoM) cycles. Lack of crucial dynamics of the biped robot, e.g., angular momentum, results in poor walking robustness [7, 8]. Nowadays, biped robot locomotion is still far from the human level.

One of the earliest simplified models that roughly describes biped locomotion is the inverted pendulum (IP) [9] with a fixed-length leg. In our previous works, we proposed a biped locomotion method with minimal energy [10],

variable speed [11], and torso swing [12] to generate natural biped walkers inspired by IP. However, numerical integration is unavoidable. Based on IP, Kajita et al. proposed the linear inverted pendulum (LIP) [13]. With additional zero moment point (ZMP) control [14], many position-controlled humanoid robots can walk stably through inverse kinematics. Nevertheless, it should be noted that humanoid robots using LIP usually have to crouch their knees to keep the CoM at a constant height [1, 2, 5]. The vertical condition of the robot can affect its balance ability and energy efficiency, e.g., it is easier to balance when the CoM is lower, and improve walking robustness by briefly raising the height of the CoM [15, 16].

There are various abstract models: Figure. 1 shows the prevailing simplified model nowadays. Apart from the models developed from IP, there are other nonlinear multi-link pendulums such as 7-link model [17]. These models are more accurate and allow for the vertical motion. Their distinguishing feature lies in the addition of links representing the limbs for geometric similarities, resulting in a higher number of degrees of freedom (DoFs) and increased complexity in the models. Currently, these models primarily focus on the planar motion of robots. The previously mentioned categories primarily explore energetic and geometric similarities. Another category, centered around the spring loaded inverted pendulum (SLIP) [18], delves into additional aspects such as ground reaction force (GRF) and elastic behaviors. The vertical motion is also allowed. To capture the characteristics of human walking more accurately, a torso is incorporated into the SLIP [19], and a passive spring is introduced to the hip joint [20]. The most distinctive feature of such models is the utilization of springs to simulate human muscles, enabling the storage and release of energy. In this paper, however, the elastic behaviors and energy storage are not investigated. Another class of models [21, 22, 23, 24], evolving from the IP, focuses on the primary characteristics of human walking, such as the shifting of the CoM and the movement of the torso. The motion of the torso rotation is beneficial to improving the stability and efficiency of walking [12]. More importantly, the rotation motion of the torso cannot be neglected in the implementation of complex locomotion, such as bending underneath an obstacle and turning. Indeed, the multi-link model may well describe the dynamics of biped locomotion. However, finding a periodic gait for such a multidimensional model is complex and computationally expensive. For real-time biped control, simplified models are instrumental in producing locomotion [2]. However, for dealing with variable CoM height locomotion and effective steering, a new reliable simplified model is suggested to abstractly determine the overall dynamics.

In this paper, we introduce a full 3D template model named *full centroid dynamics inverted pendulum* (FCDIP), which can perform flexibility and adaptability while navigating a complex world. The model helps to produce more natural motions in different scenarios, resembling human locomotion. FCDIP comprises two mass-less legs and a 3D rotating flywheel that mainly captures torso translational and rotational motion, as shown in Fig. 1. The torso accounts for most of the robot's mass and inertia. Therefore, capturing the main characteristics of the torso can approximately describe the dynamics of the biped robot [25]. Compared to LIPF [21] and VIP [23]/NIPF [24], FCDIP not only supports vertical motion but also specifically accommodates the yaw motion of the torso. This is in line with observations regarding human walking, where the height of the pelvis changes with time and describes approximately an arc when walking, to keep the mechanical energy of the torso, i.e., the sum of potential and kinetic energy, constant [26]. Some results also showed that the variable CoM height could improve the robot's walking ability, e.g., disturbance recovery capacity [16]. Moreover, the yaw dynamics of the torso of the robot are also important, especially while steering or running [27]. In FCDIP, the vertical and yaw dynamics are considered, therefore, it can generate more natural biped locomotion and perform more tasks. In brief, the FCDIP is an advanced version developed from LIP and LIPF. Moreover, we aim to explain the stable conditions of yaw motion as ZMP does in a straight motion. A new criterion (or constraint) named zero frictional moment point (ZFMP) is proposed for yaw motion stability. The ZFMP is defined as the point where the vertical component of the moment of the GRF becomes zero. With ZMP and ZFMP constraints, the nonlinear model predictive control (NMPC) automatically generates the biped locomotion trajectory, allowing the robot to perform the tasks without falling. Usually, it is challenging to complete nonlinear optimization effectively, but the closed-form formulation allows the gradient and the Hessian of the SQP to be calculated numerically in this case. In comparison to NMPC implementations in other studies, such as those by Heerden [16], Ding et al. [24], and Negri et al. [28], the inclusion of the FCDIP and ZFMP constraint within NMPC allows for the execution of additional tasks for biped robots, such as stable steering.

The FCDIP is a six-dimensional model that allows 3D translation and rotation. However, a complicating factor here is that the horizontal and vertical motion is coupled in ZMP dynamics, resulting in the dynamics being nonlinear. In this paper, unlike other typical linear ZMP dynamics strategies [13, 30, 31, 32], we treat the ZMP constraint as a quadratic constraint instead of the linear constraint for including the vertical CoM motion. Then, the related

	[9] IP	[13] LIP	[17] 7−link model	[29] −
name	IP	LIP	7−link model	−
3D	+	+	−	+
torso	−	−	+	−
variable height	+	−	+	+
yaw	−	−	−	−

	[2] 3LP	[18] SLIP	[19] TSLIP	[20] FMCH
name	3LP	SLIP	TSLIP	FMCH
3D	+	−	−	−
torso	+	−	+	+
variable height	−	+	+	+
yaw	−	−	−	−

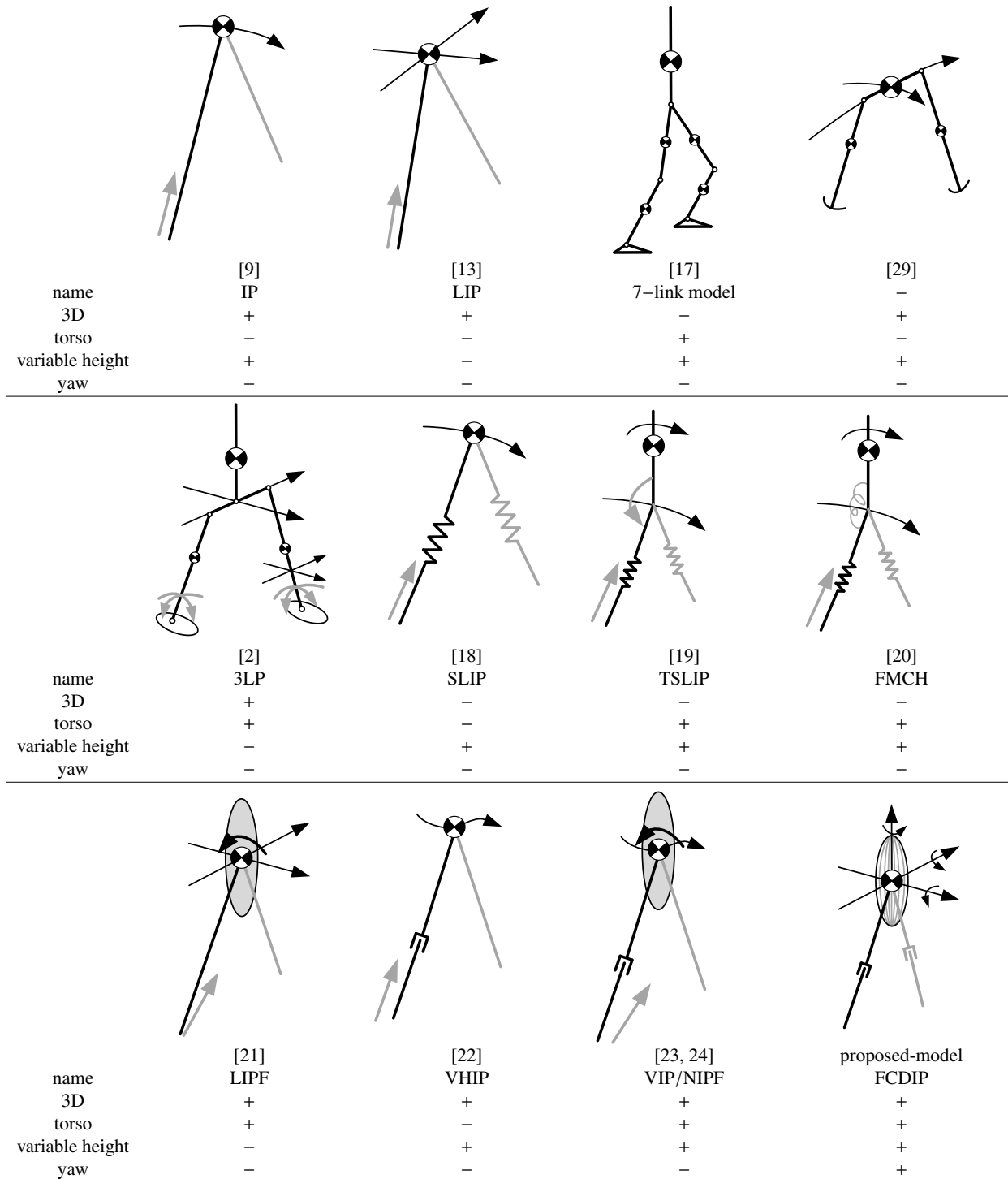|	[21] LIPF	[22] VHIP	[23, 24] VIP/NIPF	proposed-model FCDIP
name	LIPF	VHIP	VIP/NIPF	FCDIP
3D	+	+	+	+
torso	+	−	+	+
variable height	−	+	+	+
yaw	−	−	−	+

Figure 1: Different abstract models introduced in the literature for walking. For models without swing dynamics, we treat the swing leg in a grey colour. We point out some important features such as the 3D model, inclusion of the torso, variable CoM height and yaw motion. Note that, some models are only in 2D while some are in 3D. Some linear models do not allow the vertical motion for dynamics decoupling, such as LIP. Many of these models do not include the torso or do not allow for torso yaw, however, FCDIP can describe the roll, yaw and pitch motion of the robot. Overall, FCDIP offers more DoFs that do not exist in other abstract models, particularly, it includes the yaw motion.

optimization can be expressed in closed form as a nonlinear constrained quadratic program other than a quadratic program. As a result, the CoM trajectory, torso angle, and footholds are formulated through the NMPC framework with the sequential quadratic program (SQP) strategy. SQP is a well-known strategy in the aviation and vehicle industry for solving nonlinear constraints issues, and some results for the humanoid robot have been detailed in [28, 33].

Currently, most of the work in biped locomotion using ZMP does not deal with variable-height walking. Besides, the yaw motion is independent of the ZMP, i.e., the ZMP cannot guarantee yaw stability. According to the ZMP criterion [14], ZMP only guarantees that the feet cannot be rolled over, but it cannot affirm the presence of the yaw rotation motion of the feet. To avoid the rotation and slipping of the support sole due to the insufficient friction moment between the support foot sole and the floor, a few works have been discussed for yaw moment compensation [34, 35, 36, 37, 38, 39, 40, 41]. Among them, to suppress the yaw moment, the upper body motion, e.g., arms swing motion [36, 38] and waist rotation motion [34, 35, 38, 39], is controlled for yaw compensation. However, it needs extra operation for the precise motion of the waist and arm for yaw moment compensation. In [41], a bevel-geared mechanical bioinspired robotic foot was presented to emulate the rotational motions of the human subtalar and oblique midtarsal joints. From their proposed figures of the foot, so many DoFs result in an extremely complex structure. More importantly, few of them have discussed the actual friction on the soles of the feet detailedly. Zhu et al. [42] explained the real friction, including the vertical frictional moment in biped walking. The mechanism of slipping with rotation was also introduced. Regrettably, the yaw stability criterion was not discussed. In [36], similar to [42], the nature of the ZMP and yaw moment is explained. Moreover, a threshold is set for that if the angular momentum mostly exceeds the predefined threshold, the residual motion of the links is triggered to slow down by the compensation. However, the rule for setting the threshold was not specified. This threshold is, in a sense, a constraint. In this paper, the yaw motion stability constraint is explained to address the limitations of ZMP.

With the above considerations in mind, the main contributions of this work are listed below.

- A new 3D biped abstract model is proposed. The proposed model allows six dimensional motion, including three dimensional translation and three dimensional rotation. In particular, it accounts for vertical translation and rotation which are often overlooked in other locomotion research [3, 19, 24].

- A new additional stability criterion, the ZFMP, is introduced. The ZFMP is proposed to guarantee stable natural steering without foot yaw rotation.

The remainder of this paper is structured in the following manner. In Section 2, we introduce the dynamics of FCDIP. Then, the nonlinear ZMP dynamics and ZFMP are explained. Section 3 presents the trajectory generation method using NMPC to obtain stable locomotion. Moreover, the SQP is also explained. Some simulations, e.g., walking underneath the low door and steering, are reported in Section 5. Section 6 provides the discussion and conclusion.

2. FCDIP dynamics

This section is devoted to simplifying the biped robot mathematical model and introducing the proposed FCDIP model. Moreover, its stability criterion will be discussed.

2.1. Evaluation of the FCDIP

Traditionally, the biped robot can be approximated easily as an imaginary 3D LIP, which consists of the CoM and a massless leg connecting the CoM and the supporting point. Later, this model is extended to LIPF with rotational inertia. With the acceleration of the CoM and angular momentum stored in the flywheel, the ZMP location's coordinates $[p_x, p_z]^{\mathrm{T}} \in \mathbb{R}^2$ is given as [21]

$$p_x = c_x - \frac{c_y}{g}\ddot{c}_x - \frac{\dot{L}_z}{mg}, \tag{1}$$

$$p_z = c_z - \frac{c_y}{g}\ddot{c}_z + \frac{\dot{L}_x}{mg}, \tag{2}$$

where $[c_x, c_z]^T \in \mathbb{R}^2$ are the CoM's coordinates in the horizontal plane, $c_y \in \mathbb{R}$ represents the vertical height of the CoM, $[L_x, L_z]^T \in \mathbb{R}^2$ denotes the angular momentum's coordinates around the x - and z-axes, respectively, $m > 0$ is the mass, and $g \simeq 9.81$ m/s^2 is the gravity acceleration. Herein, to deal with variable CoM's height due to the variable-height base, the friction force coordinates, $[f_x, f_z]^T \in \mathbb{R}^2$, and the ZMP location (see Fig. 2) can be expressed as

$$f_x = m\ddot{x}, \quad f_z = m\ddot{z}, \tag{3}$$

$$p_x = c_x - \frac{c_y - s_y}{\ddot{c}_y + g}\ddot{c}_x - \frac{J_z\ddot{\theta}_z}{m(g + \ddot{c}_y)}, \quad p_z = c_z - \frac{c_y - s_y}{\ddot{c}_y + g}\ddot{c}_z + \frac{J_x\ddot{\theta}_x}{m(g + \ddot{c}_y)}, \tag{4}$$

where $s_y \in \mathbb{R}$ is the height of the support polygon, $[J_x, J_z]^T \in \mathbb{R}^2$ is inertia around the x - and z-axes, respectively, and $[\theta_x, \theta_z]^T \in \mathbb{R}^2$ is the roll and pitch angles of the torso, respectively.

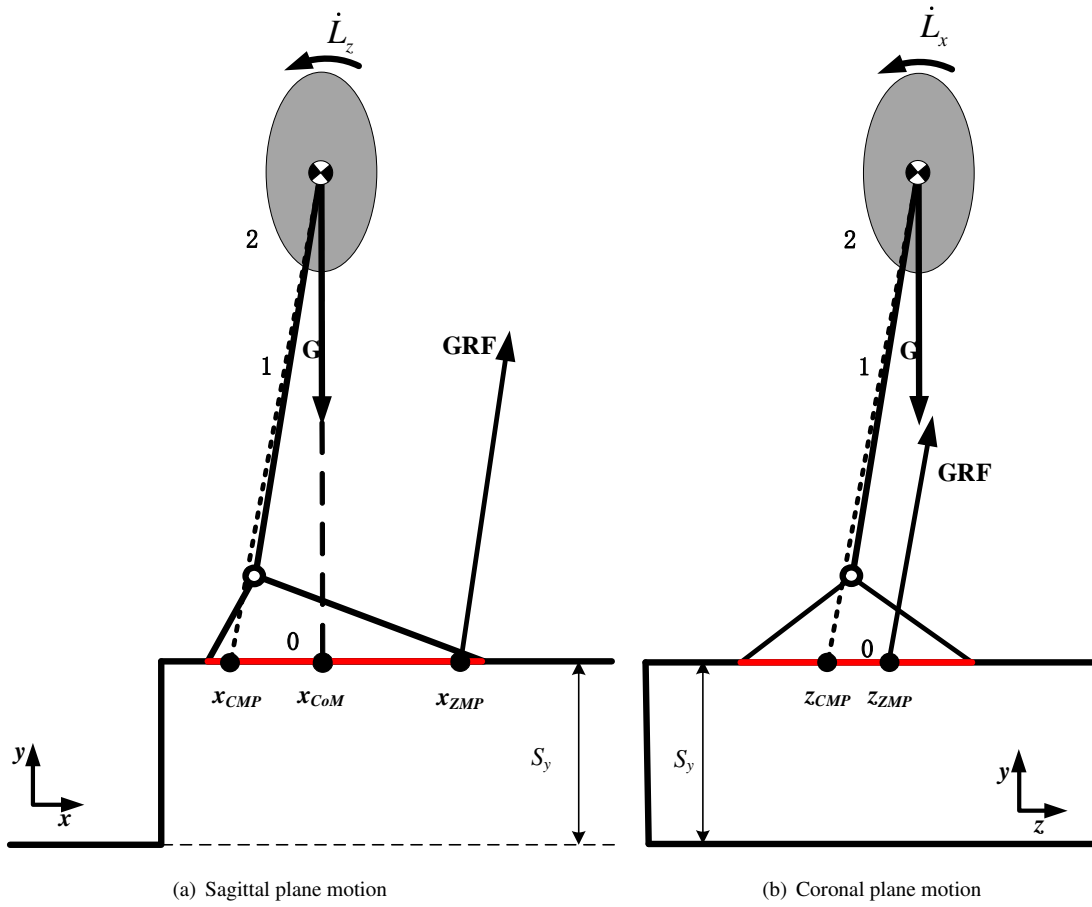(a) Sagittal plane motion   (b) Coronal plane motion

Figure 2: ZMP dynamics on the uneven terrain. If the configuration of the foot is rectangular, ZMP should be within the red line in each plane.

For stable walking without foot rotation, the ZMP should be inside the support polygon [14], which is determined by the geometry of the supporting feet.

2.2. ZFMP for yaw motion stability

The ZMP expression in (4) appears independent from the yaw motion. Consider the condition of the single support phase: according to the definition of the ZMP [14], this is the point where the moment of the horizontal component
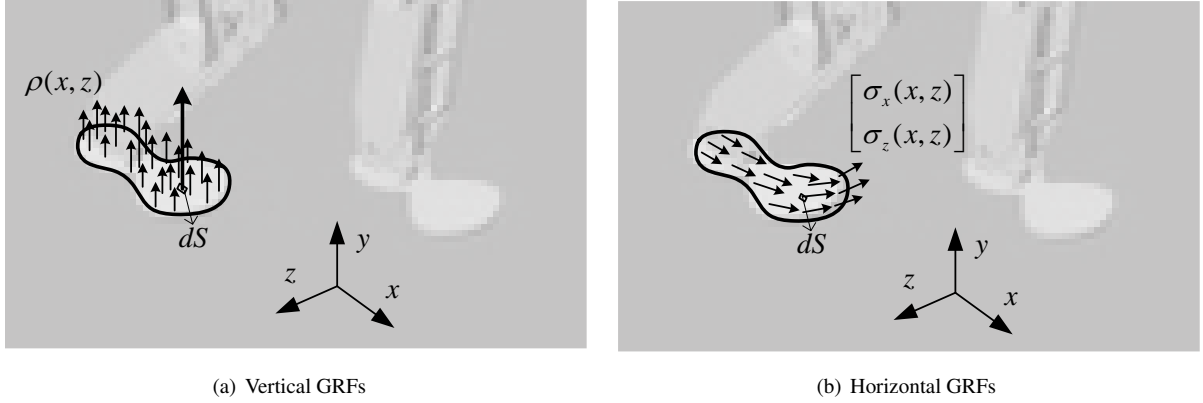
(a) Vertical GRFs   (b) Horizontal GRFs

Figure 3: GRF in 3D

of the GRF becomes zero, as shown in Fig. 3, then

$$p_x = \frac{\int_S x\rho(x,z)dS}{\int_S \rho(x,z)dS}, \tag{5}$$

$$p_z = \frac{\int_S z\rho(x,z)dS}{\int_S \rho(x,z)dS}, \tag{6}$$

where $\rho(x,z)$ is the pressure over the surface of the sole, S. In other words, the ZMP is equivalent to the center of pressure (CoP), $\boldsymbol{p} = \begin{bmatrix} p_x, p_y, p_z \end{bmatrix}^T \in \mathbb{R}^3$. Let $\boldsymbol{\tau}_p = \begin{bmatrix} \tau_{px} & \tau_{py} & \tau_{pz} \end{bmatrix}^T \in \mathbb{R}^3$ be the ground reaction moment around the ZMP, where $\tau_{px} = 0$, $\tau_{pz} = 0$, and the vertical component equal to

$$\tau_{py} = \int_S \{(x - p_x)\,\sigma_z(x,z) - (z - p_z)\,\sigma_x(x,z)\}\,dS. \tag{7}$$

In the previous section, we pointed out that the motion in the sagittal and coronal planes can determine the friction forces and the ZMP location. In the translation direction, the resultant friction force must be inside the friction angle to avoid the slide. Besides, the vertical moment generated by the friction cannot be an arbitrary value in practice as the contact surface is geometrically bounded. That is, it must have a threshold. According to Newton's law, the yaw motion of the robot generates the vertical component of the ground reaction moment at the ZMP, and the force/moment applied by the robot to the ground can be obtained by

$$\boldsymbol{f}_p = m(\boldsymbol{g} - \ddot{\boldsymbol{c}}), \tag{8}$$

$$\boldsymbol{\tau}_p = -\dot{\boldsymbol{L}}_c + m(\boldsymbol{c} - \boldsymbol{p}) \times (\boldsymbol{g} - \ddot{\boldsymbol{c}}), \tag{9}$$

where $\boldsymbol{L}_c = \begin{bmatrix} L_x, L_y, L_z \end{bmatrix}^T \in \mathbb{R}^3 \in \mathbb{R}^3$ denotes the angular momentum about the CoM, $\boldsymbol{c} = \begin{bmatrix} c_x, c_y, c_z \end{bmatrix}^T \in \mathbb{R}^3$ is the full CoM location, $\boldsymbol{g} = [0, -g, 0]^T \in \mathbb{R}^3$ is the gravity vector, and the symbol $\times$ denotes the vector product. Herein, we propose a new indication point, the ZFMP, which represents the point where the vertical moment becomes zero thus complementing the standard ZMP criterion. Indeed, tribology, as a scientific discipline, has a long history of research. However, it is not fully understood yet due to its complexity [43]. Here, thanks to the simplification of the robot in FCDIP, the friction force is determined by the horizontal motion of the CoM. If the CoM lacks rotational moment, the GRF should pass directly through the CoM, and ZFMP should be at the intersection of the GRF and the ground in the horizontal plane. ZFMP starts to move when the CoM experiences a rotational moment. The maximum movement is constrained by the support polygon formed by the foot and the ground, reaching the maximum yaw moment once it moves to the edge of the foot. Thus, the ZFMP must be on the line expressed as

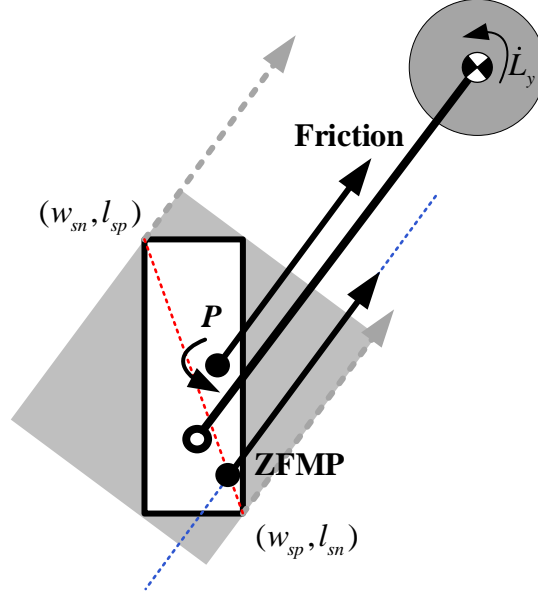$$m\ddot{c}_z x - m\ddot{c}_x z + \dot{L}_y - m\ddot{c}_z c_x + m\ddot{c}_x c_z = 0. \tag{10}$$

6

Figure 4: The friction force and moment are applied to the foot. The friction force must be within the scope between the two dashed arrows to avoid foot yaw rotation. At any point on the blue dashed line, the friction moment is zero. However, only some of the points on the blue dashed line are within the support polygon formed by the foot and the ground. To further determine the position of ZFMP, we take the two points farthest from the vertical distance on both sides of the friction force at the ankle. Then, we connect these two points with a line, represented by the red dotted line. The intersection of the blue dotted line and the red dotted line indicates the location of ZFMP. Note that, the upper and lower bound of the support polygon's length and width in this case is obtained by the two point.

Figure 4 illustrates how to determine ZFMP at the case of the components of friction in the x and y directions are both positive or negative. Given the upper and lower bound of the support polygon's length $l_{sp}, l_{sn} \in \mathbb{R}$ and width $w_{sp}, w_{sn} \in \mathbb{R}$, the diagonal line of the support polygon is

$$\frac{z - l_{sp}}{l_{sn} - l_{sp}} - \frac{x - w_{sn}}{w_{sp} - w_{sn}} = 0. \tag{11}$$

Here, we specify the ZFMP is the intersection of the two lines. Then, the ZFMP could be expressed as

$$x = \left(\frac{\ddot{c}_z}{\ddot{c}_z - \ddot{c}_x k_d}\right)\left(\ddot{c}_x - \frac{\ddot{c}_x (c_z - b_d)}{\ddot{c}_z} - \frac{\dot{L}_y}{m \ddot{c}_z}\right), \tag{12}$$

where $k_d = (l_{sp} - l_{sn})/(w_{sp} - w_{sn})$ and $b_d = l_{sp} - k_d w_{sn}$.

The ZFMP must lie in the support polygon for stable walking without sliding. Hence, taking components of friction in the x and y directions are both positive or negative as an example (Fig. 4), the yaw moment must satisfy the constraint as follows

$$w_{sn} m \ddot{c}_x - l_{sp} m \ddot{c}_z \leq \dot{L}_y \leq w_{sp} m \ddot{c}_x - l_{sn} m \ddot{c}_z, \tag{13}$$

3. Optimization based on NMPC

In this section, we formulate an NMPC problem to find stabilizing locomotion for the robot. The controller inputs are the jerks of the six-dimensional motion of the CoM and footholds.

3.1. Definitions and common nomenclature

Assume the CoM motions to have piece-wise constant jerks $\dddot{c}_w \in \mathbb{R}$ and $\dddot{\theta}_w \in \mathbb{R}$ over time intervals of constant length $T > 0$. In this paper, the $x - z$ plane is the horizontal plane and the y axes are the vertical direction. The letter

w is used to succinctly represent the symbols x, y, or z in equations that apply to different axes. Hence, $w \in \{x, y, z\}$, and the corresponding dynamics of the CoM at discrete time $t_k = kT$, with $k \in \mathbb{Z}$, are

$$\hat{\boldsymbol{c}}_{k+1}^w = \hat{\boldsymbol{c}}_w(t_{k+1}) = \boldsymbol{A}\hat{\boldsymbol{c}}_w(t_k) + \boldsymbol{B}\,\dddot{c}_w(t_k),$$
$$\hat{\boldsymbol{\theta}}_{k+1}^w = \hat{\boldsymbol{\theta}}_w(t_{k+1}) = \boldsymbol{A}\hat{\boldsymbol{\theta}}_w(t_k) + \boldsymbol{B}\,\dddot{\theta}_w(t_k),$$

(14)

with

$$\hat{\boldsymbol{c}}_k^w = \begin{pmatrix} c_w(t_k) \\ \dot{c}_w(t_k) \\ \ddot{c}_w(t_k) \end{pmatrix}, \quad \hat{\boldsymbol{\theta}}_k^w = \begin{pmatrix} \theta_w(t_k) \\ \dot{\theta}_w(t_k) \\ \ddot{\theta}_w(t_k) \end{pmatrix},$$

(15)

and

$$\boldsymbol{A} = \begin{pmatrix} 1 & T & T^2/2 \\ 0 & 1 & T \\ 0 & 0 & 1 \end{pmatrix}, \quad \boldsymbol{B} = \begin{pmatrix} T^3/6 \\ T^2/2 \\ T \end{pmatrix}.$$

(16)

Let $\tilde{\boldsymbol{c}}_k^w = \begin{bmatrix} c_{k+1}^w, \cdots, c_{k+N_h}^w \end{bmatrix}^{\mathrm{T}} \in \mathbb{R}^{N_h}$ and $\tilde{\boldsymbol{\theta}}_k^w = \begin{bmatrix} \theta_{k+1}^w, \cdots, \theta_{k+N_h}^w \end{bmatrix}^{\mathrm{T}} \in \mathbb{R}^{N_h}$ be the CoM translation and rotation trajectories at either coordinate over $N_h > 0$ time intervals of the discretized system, respectively. Hence, the CoM translation trajectory vector can be defined as $\chi_k = \begin{bmatrix} \tilde{\boldsymbol{c}}_k^x; \tilde{\boldsymbol{c}}_k^y; \tilde{\boldsymbol{c}}_k^z \end{bmatrix} \in \mathbb{R}^{3N_h}$. To ease the notation, we use the compact form $[\boldsymbol{a}; \boldsymbol{b}]^{\mathrm{T}} = \begin{bmatrix} \boldsymbol{a}^{\mathrm{T}}, \boldsymbol{b}^{\mathrm{T}} \end{bmatrix}^{\mathrm{T}}$, where $\boldsymbol{a}, \boldsymbol{b}$ are to generic vectors, to stack vectors in column. Similarly, let $\boldsymbol{\vartheta}_k = \begin{bmatrix} \tilde{\boldsymbol{\theta}}_k^x; \tilde{\boldsymbol{\theta}}_k^y; \tilde{\boldsymbol{\theta}}_k^z \end{bmatrix} \in \mathbb{R}^{3N_h}$ be the rotational angle vector. Assume there are M support phases, i.e., the left, right or double support of the robot's feet, involved in the N_h predicted time steps. Let $\boldsymbol{f}_k^w = \begin{bmatrix} f_{k+1}^{l\_w}, \cdots; f_{k+M}^{l\_w}, f_{k+1}^{r\_w}, \cdots, f_{k+M}^{r\_w} \end{bmatrix}^{\mathrm{T}} \in \mathbb{R}^{2M}$ where $f_{k+i}^{l\_w} \in \mathbb{R}$ and $f_{k+i}^{r\_w} \in \mathbb{R}$ are the left and right foot locations at either coordinate during the i-th support phase which belongs to the locomotion at the time k, respectively. As a result, the foot location vector can be defined as $\boldsymbol{F}_k = \begin{bmatrix} f_k^x; f_k^y; f_k^z \end{bmatrix} \in \mathbb{R}^{6M}$ Finally, the input vector at time k, $\boldsymbol{u}_k \in \mathbb{R}^{N_t}$, with $N_t = 6N_h + 6M$, is expressed as

$$\boldsymbol{u}_k = \begin{bmatrix} \dddot{\chi}_k; \dddot{\boldsymbol{\vartheta}}_k; \boldsymbol{F}_k \end{bmatrix} = \begin{bmatrix} \dddot{\boldsymbol{c}}_k^x; \dddot{\boldsymbol{c}}_k^y; \dddot{\boldsymbol{c}}_k^z; \dddot{\boldsymbol{\theta}}_k^x; \dddot{\boldsymbol{\theta}}_k^y; \dddot{\boldsymbol{\theta}}_k^z; \boldsymbol{f}_k^x; \boldsymbol{f}_k^y; \boldsymbol{f}_k^z \end{bmatrix}.$$

(17)

Besides, let $\boldsymbol{S}_f^w \in \mathbb{R}^{2M \times N_t}$, $\boldsymbol{S}_\theta^w \in \mathbb{R}^{N_h \times N_t}$, $\boldsymbol{S}_j^w \in R^{N_h \times N_t}$, and $\boldsymbol{S}_i \in \mathbb{R}^{1 \times N_h}$ be the selection matrices to extract the foot location and CoM jerk from the input vector

$$\boldsymbol{f}_k^w = \boldsymbol{S}_f^w \boldsymbol{u}_k,$$

(18)

$$\dddot{\boldsymbol{\theta}}_k^w = \boldsymbol{S}_\theta^w \boldsymbol{u}_k,$$

(19)

$$\dddot{\boldsymbol{c}}_k^w = \boldsymbol{S}_j^w \boldsymbol{u}_k,$$

(20)

$$\dddot{c}_{k+i}^w = \boldsymbol{S}_i \dddot{\boldsymbol{C}}_k^w.$$

(21)

Using (14) recursively, the position, velocity and acceleration of the CoM at time $k + i$ can be expressed as

$$c_{k+i}^w = \boldsymbol{S}_i \boldsymbol{P}_{ps} \hat{\boldsymbol{c}}_k^w + \boldsymbol{S}_i \boldsymbol{P}_{pu} \boldsymbol{S}_j^w \boldsymbol{u}_k,$$
$$\dot{c}_{k+i}^w = \boldsymbol{S}_i \boldsymbol{P}_{vs} \hat{\boldsymbol{c}}_k^w + \boldsymbol{S}_i \boldsymbol{P}_{vu} \boldsymbol{S}_j^w \boldsymbol{u}_k,$$
$$\ddot{c}_{k+i}^w = \boldsymbol{S}_i \boldsymbol{P}_{as} \hat{\boldsymbol{c}}_k^w + \boldsymbol{S}_i \boldsymbol{P}_{au} \boldsymbol{S}_j^w \boldsymbol{u}_k.$$

(22)

Similarly, the conditions of the rotational angle are given as

$$\theta_{k+i}^w = \boldsymbol{S}_i \boldsymbol{P}_{ps} \hat{\boldsymbol{\theta}}_k^w + \boldsymbol{S}_i \boldsymbol{P}_{pu} \boldsymbol{S}_\theta^w \boldsymbol{u}_k,$$
$$\dot{\theta}_{k+i}^w = \boldsymbol{S}_i \boldsymbol{P}_{vs} \hat{\boldsymbol{\theta}}_k^w + \boldsymbol{S}_i \boldsymbol{P}_{vu} \boldsymbol{S}_\theta^w \boldsymbol{u}_k,$$
$$\ddot{\theta}_{k+i}^w = \boldsymbol{S}_i \boldsymbol{P}_{as} \hat{\boldsymbol{\theta}}_k^w + \boldsymbol{S}_i \boldsymbol{P}_{au} \boldsymbol{S}_\theta^w \boldsymbol{u}_k.$$

(23)

The matrices $\boldsymbol{P}_{ps}$, $\boldsymbol{P}_{vs}$ and $\boldsymbol{P}_{av} \in \mathbb{R}^{N_h \times 3}$ and $\boldsymbol{P}_{pu}$, $\boldsymbol{P}_{vu}$ and $\boldsymbol{P}_{au} \in \mathbb{R}^{N_h \times N_h}$ introduced here are determined directly from the recursive application of the CoM dynamics. The detailed expression of these matrices are shown in the Appendix A.

3.2. Optimization objective formulation

To obtain a smooth trajectory with low energy consumption, the jerks $\dddot{\chi}_k$ and $\dddot{\vartheta}_k$ need to be minimized for stable walking over a prediction time horizon of $N_h T$ with the tacking of the reference positions and angles given by $\chi_k^{ref} = [\bar{c}_k^x; \bar{c}_k^y; \bar{c}_k^z]$ and $\vartheta_k^{ref} = [\bar{\theta}_k^x; \bar{\theta}_k^y; \bar{\theta}_k^z]$, respectively. Besides, to minimize the errors between the desired and actual foot locations as well as between the velocity of the CoM, the following cost function is designed

$$
\min_{u_k} \frac{\alpha_p}{2} \left\| \chi_k - \chi_k^{ref} \right\|^2 + \frac{\alpha_v}{2} \left\| \dot{\chi}_k \right\|^2 + \frac{\alpha_j}{2} \left\| \dddot{\chi}_k \right\|^2 + \frac{\beta_p}{2} \left\| \vartheta_k - \vartheta_k^{ref} \right\|^2
$$
$$
+ \frac{\beta_v}{2} \left\| \dot{\vartheta}_k \right\|^2 + \frac{\beta_j}{2} \left\| \dddot{\vartheta}_k \right\|^2 + \frac{\gamma}{2} \left\| F_k - F_k^{ref} \right\|^2 . \tag{24}
$$

This optimization formulation with some constraints, namely, the quadratically constrained quadratic programming (QCQP), can be expressed canonically as[16, 30, 31]

$$
\min_{u_k} \psi(u_k) = u_k^{\mathrm{T}} Q u_k + q_k^{\mathrm{T}} u_k
$$
$$
\text{s.t.}
$$
$$
h_i(u_k) \leq 0, \tag{25}
$$
$$
h_{nl,i}(u_k) = u_k^{\mathrm{T}} P_i u_k + p_i^{\mathrm{T}} u_k + \sigma_i,
$$
$$
h_{l,i}(u_k) = v_i^{\mathrm{T}} u_k + \rho_i, \quad 1 \leq i \leq N_k,
$$

where $h_i(u_k)$ represents an inequality constraint later detailed, $h_{nl,i}(u_k)$ and $h_{l,i}(u_k)$ are the nonlinear and linear constraints, respectively; $P_i \in \mathbb{R}^{N_t \times N_t}$, $p_i \in \mathbb{R}^{N_t}$ and $\sigma_i \in \mathbb{R}$ are parameters specifying the nonlinear constraints; similarly, $v_i \in \mathbb{R}^{N_t}$ and $\rho_i \in \mathbb{R}$ are parameters specifying the linear constraints; $\alpha_p, \alpha_v, \alpha_j > 0$ and $\beta_p, \beta_v, \beta_j > 0$ are the position tracking, velocity, and jerk penalty terms of the CoM translation and rotation motion, respectively; $\gamma > 0$ is the foot-tracking penalty term. These penalties are positive so that the Hessian matrix $Q \in \mathbb{R}^{N_t \times N_t}$ is positive-definite, and Q can be formulated in the following quadratic form

$$
Q = \text{blkdiag}\left(\psi_x, \psi_y, \psi_z, \varphi_x, \varphi_y, \varphi_z, \phi_x, \phi_y, \phi_z \right),
$$
$$
\psi_w = \frac{\alpha_j}{2} I^{N_h \times N_h} + \frac{\alpha_v}{2} P_{vu}^{\mathrm{T}} P_{vu} + \frac{\alpha_p}{2} P_{pu}^{\mathrm{T}} P_{pu},
$$
$$
\varphi_w = \frac{\beta_j}{2} I^{N_h \times N_h} + \frac{\beta_v}{2} P_{vu}^{\mathrm{T}} P_{vu} + \frac{\beta_p}{2} P_{pu}^{\mathrm{T}} P_{pu}, \tag{26}
$$
$$
\phi_w = \frac{\gamma}{2} I^{2M \times 2M},
$$

where $\text{blkdiag}(x)$ construct a block diagonal matrix. The vector $q_k \in \mathbb{R}^{N_t}$ in (25) is expressed as

$$
q_k = \begin{bmatrix}
\alpha_{px} P_{pu}^{\mathrm{T}} P_{ps} \hat{c}_k^x + \alpha_{vx} P_{vu}^{\mathrm{T}} P_{vs} \hat{c}_k^x - \alpha_{px} P_{pu}^{\mathrm{T}} \bar{c}_k^x \\
\alpha_{py} P_{pu}^{\mathrm{T}} P_{ps} \hat{c}_k^y + \alpha_{vy} P_{vu}^{\mathrm{T}} P_{vs} \hat{c}_k^y - \alpha_{py} P_{pu}^{\mathrm{T}} \bar{c}_k^y \\
\alpha_{pz} P_{pu}^{\mathrm{T}} P_{ps} \hat{c}_k^z + \alpha_{vx} P_{vu}^{\mathrm{T}} P_{vs} \hat{c}_k^z - \alpha_{pz} P_{pu}^{\mathrm{T}} \bar{c}_k^z \\
\beta_{px} P_{pu}^{\mathrm{T}} P_{ps} \hat{\theta}_k^x + \beta_{vx} P_{vu}^{\mathrm{T}} P_{vs} \hat{\theta}_k^x - \beta_{px} P_{pu}^{\mathrm{T}} \bar{\theta}_k^x \\
\beta_{py} P_{pu}^{\mathrm{T}} P_{ps} \hat{\theta}_k^y + \beta_{vy} P_{vu}^{\mathrm{T}} P_{vs} \hat{\theta}_k^y - \beta_{py} P_{pu}^{\mathrm{T}} \bar{\theta}_k^y \\
\beta_{pz} P_{pu}^{\mathrm{T}} P_{ps} \hat{\theta}_k^z + \beta_{vx} P_{vu}^{\mathrm{T}} P_{vs} \hat{\theta}_k^z - \beta_{pz} P_{pu}^{\mathrm{T}} \bar{\theta}_k^z \\
-\gamma_x \bar{f}_k^x \\
-\gamma_y \bar{f}_k^y \\
-\gamma_z \bar{f}_k^z
\end{bmatrix} . \tag{27}
$$

The detailed processes of derivation to obtain Q and q_k are shown in Appendix B.

The reference footholds $\left[\bar{f}_k^x; \bar{f}_k^y; \bar{f}_k^z \right]$ according to environmental conditions needs to be supplied in advance. Similarly, the user should also supply the reference height of the CoM and the rotational angle of the torso. To simplify the

calculation, the CoM reference position is associated with the central position of the supporting foot of each period, i.e., the foothold of each period

$$\bar{c}_k^w = \left[\bar{c}_{k+1}^w, \ldots, \bar{c}_{k+N_h}^w\right]^{\mathrm{T}} = US_{fc}^w u_k, \tag{28}$$

where $U \in \mathbb{R}^{N_h \times 2M}$ is a selection matrix mapping the left and right footholds at the different phases into the support polygon centers over the prediction horizon of length $N_h T$. Here, we take the prediction time, which just successively includes the single support of the left foot, the double support, and the single support of the right foot, as an example. The U can be expressed as

$$U = \begin{bmatrix} \mathbf{1}^{1\times m_{sp}} & \mathbf{0}^{1\times n_{dp}} & \mathbf{0}^{1\times m_{sp}} \\ \mathbf{0}^{1\times m_{sp}} & \mathbf{0.5}^{1\times n_{dp}} & \mathbf{0}^{1\times m_{sp}} \\ \mathbf{0}^{1\times m_{sp}} & \mathbf{0}^{1\times n_{dp}} & \mathbf{0}^{1\times m_{sp}} \\ \mathbf{0}^{1\times m_{sp}} & \mathbf{0}^{1\times n_{dp}} & \mathbf{0}^{1\times m_{sp}} \\ \mathbf{0}^{1\times m_{sp}} & \mathbf{0.5}^{1\times n_{dp}} & \mathbf{0}^{1\times m_{sp}} \\ \mathbf{0}^{1\times m_{sp}} & \mathbf{0}^{1\times n_{dp}} & \mathbf{1}^{1\times m_{sp}} \end{bmatrix}^{\mathrm{T}}, \tag{29}$$

where $\mathbf{1}^{1\times m_{sp}}$ and $\mathbf{0.5}^{1\times n_{dp}}$ are a $1 \times m$ row vector filled with ones and a $1 \times n$ vector row filled with 0.5, respectively; while m_{sp} and n_{dp} are determined by the single and double support duration, t_{sp} and t_{dp}, as

$$\begin{aligned} t_{sp} &= m_{sp}T, \\ t_{dp} &= n_{dp}T. \end{aligned} \tag{30}$$

3.3. Feasibility constraints

To ensure the feasibility of the generated gait, the feasibility constraints, that is, ZMP and ZFMP stability constraints, foothold range limitations and hip torque limitations need to be considered.

3.3.1. ZMP constraints with variable CoM height

According to the ZMP criterion [14], the ZMP needs to be inside the support polygon to guarantee that the biped robot's locomotion is physically reliable. Here, we take the ZMP in the x-direction as an example

$$c_{k+i}^x + l_{sn} \le p_{k+i}^x \le c_{k+i}^x + l_{sp}. \tag{31}$$

Here, we just consider the upper bound of the ZMP constraint while multiplying $(\ddot{c}_{k+i} + g)$ and substitute (3) into (41). Then, we obtain the following quadratic constraint

$$c_{k+i}^x \ddot{c}_{k+i}^y + c_{k+i}^x g - c_{k+i}^y \ddot{c}_{k+i}^x + \bar{s}_{k+i}^y \ddot{c}_{k+i}^x - \frac{J_z}{m}\ddot{\theta}_{k+i}^z - \bar{s}_{k+i}^x \ddot{c}_{k+i}^y - l_{sp}\ddot{c}_{k+i}^y - \bar{s}_{k+i}^x g - l_{sp}g \le 0. \tag{32}$$

The lower bound of the ZMP can be considered similarly: substituting (18) into (32) and collecting the terms and kneading them into a neat frame, the ZMP constraints in (25) can be expressed as

$$\begin{aligned}
\eta_{i,x} &= \left(S_j^x\right)^{\mathrm{T}} P_{pu}^{\mathrm{T}} S_i^{\mathrm{T}} S_i P_{au} S_j^y - \left(S_j^y\right)^{\mathrm{T}} P_{pu}^{\mathrm{T}} S_i^{\mathrm{T}} S_i P_{au} S_j^x + \left(S_j^x\right)^{\mathrm{T}} P_{au}^{\mathrm{T}} S_i^{\mathrm{T}} S_i US_f^y - \left(S_j^y\right)^{\mathrm{T}} P_{au}^{\mathrm{T}} S_i^{\mathrm{T}} S_i US_f^x, \\
p_{i,x}^{\mathrm{T}} &= -l_{sp}S_i P_{au} S_j^y + g P_{pu} S_j^x - \frac{J_z}{m} S_i P_{pu} S_\theta^z + gS_i US_f^x + \left(\hat{c}_k^x\right)^{\mathrm{T}} P_{ps}^{\mathrm{T}} S_i^{\mathrm{T}} S_i P_{au} S_j^y \\
&\quad + \left(\hat{c}_k^y\right)^{\mathrm{T}} P_{as}^{\mathrm{T}} S_i^{\mathrm{T}} S_i P_{pu} S_j^x - \left(\hat{c}_k^x\right)^{\mathrm{T}} P_{ps}^{\mathrm{T}} S_i^{\mathrm{T}} S_i P_{au} S_j^x - \left(\hat{c}_k^x\right)^{\mathrm{T}} P_{as}^{\mathrm{T}} S_i^{\mathrm{T}} S_i P_{pu} S_j^y \\
&\quad + \left(\hat{c}_k^x\right)^{\mathrm{T}} P_{as}^{\mathrm{T}} S_i^{\mathrm{T}} S_i US_f^y - \left(\hat{c}_k^y\right)^{\mathrm{T}} P_{as}^{\mathrm{T}} S_i^{\mathrm{T}} S_i US_f^x, \\
\sigma_{i,x} &= gS_i P_{ps}\hat{c}_k^x - \frac{J_z}{m} S_i P_{as}\hat{\theta}_k^z - l_{sp}S_i P_{as}\hat{c}_k^y - l_{sp}g + \hat{c}_k^x P_{ps}^{\mathrm{T}} S_i^{\mathrm{T}} S_i P_{as}\hat{c}_k^y - \hat{c}_k^x P_{as}^{\mathrm{T}} S_i^{\mathrm{T}} S_i P_{ps}\hat{c}_k^y.
\end{aligned} \tag{33}$$

These equations should be computed in parallel at each time step. To obtain the gradient or Hessian of the quadratic constraint form, i.e., $u_k^{\mathrm{T}} P_{i,x} u_k + p_{i,x}^{\mathrm{T}} + \sigma_{i,x}$, it is necessary to find the symmetric matrix $P_{i,x}$. However, $\eta_{i,x}$ determined

in (33) is not symmetric. Since any square matrix can be decomposed in the sum between a symmetric and a skew-symmetric matrix, the symmetric matrix $\boldsymbol{P}_{i,x}$ can be obtained by the following operation

$$\boldsymbol{P}_{i,x} = \frac{1}{2}\left(\boldsymbol{\eta}_{i,x} + \boldsymbol{\eta}_{i+x}^{\mathrm{T}}\right), i = 1, \ldots, N_h. \tag{34}$$

As a result, the upper bound of ZMP in the x-direction is added, the lower bound can be obtained by replacing l_{sp} with l_{sn} and multiplied by -1.

This process can be repeated to establish the ZMP constraints in the y-direction.

3.3.2. ZFMP for no-yaw rotation sliding

In Sec.2, we have discussed the limitation of ZMP in biped locomotion stability since it only indicates two-dimensional information of the GRF, while the dynamics of the CoM are six dimensions. Thus, we add the ZFMP criterion to ensure no slips occur during the walk. Similarly, taking the situation in Fig. 4 as an example, we also consider the upper bound of the ZFMP constraint while squaring (13), then we obtain the constraint as follows

$$J_{k+i}^{y}\ddot{\theta}_{k+i}^{y} - w_{sp}m\ddot{c}_{k+i}^{x} + l_{sn}m\ddot{c}_{k+i}^{z} \leq 0. \tag{35}$$

Here, we only take the upper and lower bounds in the single support phase as a simplification. Substituting (18) to (35), the ZFMP constraints in (25) can be expressed as

$$\begin{aligned}
\boldsymbol{v}_i^{\mathrm{T}} &= J_y\boldsymbol{S}_i\boldsymbol{P}_{au}\boldsymbol{S}_\theta^{y} - w_{sp}m\boldsymbol{S}_i\boldsymbol{P}_{au}\boldsymbol{S}_j^{x} + l_{sn}m\boldsymbol{S}_i\boldsymbol{P}_{au}\boldsymbol{S}_j^{z}, \\
\rho_i &= J_y\boldsymbol{S}_i\boldsymbol{P}_{as}\hat{\boldsymbol{\theta}}_k^{y} - w_{sp}m\boldsymbol{S}_i\boldsymbol{P}_{as}\hat{\boldsymbol{c}}_k^{x} + l_{sn}m\boldsymbol{S}_i\boldsymbol{P}_{as}\hat{\boldsymbol{c}}_k^{z}.
\end{aligned} \tag{36}$$

3.3.3. Constraints on the foot location

The actual foot landing point changes according to the current state, which is constrained by leg length, joint angular velocity, self-collision, etc.. Thus, it needs to be constrained for physical realizability.

Let us assume, without loss of generality, that the left foot is the starting support foot in the prediction horizon, followed by the double support phase and, finally, the right support one, respectively. Then, the following constraints need to be implemented

$$f_{lc}(1) = f_{lc}(2), f_{lc}(2) = f_{lc}(3), f_{rc}(2) = f_{rc}(3). \tag{37}$$

Note that the foot location in the current support phase no longer participates in optimizing

$$f_{lc}(1) = f_{lc}^{*}, f_{rc}(1) = f_{rc}^{*}, \tag{38}$$

where f_{lc}^{*} and f_{rc}^{*} are the initial location of the left and right foot at the current support phase.

Next, due to the limitation of robot structure size and actuator ability, the walking parameters such as step length and step width should be limited. Here, taking the foot location in the x-direction as an example, we can get the constraint as follows

$$f_x^{\min} \leq f_{lx}(i) - f_{rx}(i) \leq f_x^{\max}, \quad i = \{1, \ldots, M\}, \tag{39}$$

where $f_x^{\min}$ and $f_x^{\max}$ are the lower and upper boundaries of the step size constraint.

3.3.4. Other constraints

1) *CoM height constraint*: to avoid overstretching of the leg, the CoM height should be constrained within a reliable range. Similar to the ZFMP constraint, a linear constraint is applied as follows

$$y_{\min} \leq \boldsymbol{S}_i\boldsymbol{P}_{pu}\boldsymbol{S}_j^{y}\boldsymbol{u}_k + \boldsymbol{S}_i\boldsymbol{P}_{ps}\hat{\boldsymbol{c}}_k^{y} \leq y_{\max}, i \in \{1, \ldots, N_h\}, \tag{40}$$

where $y_{\min}$ and $y_{\max}$ are the minimum and maximum CoM values, respectively.

2) *Torso rotation angle and torque constraint*: the rotation range of the torso is limited by the structure size and driving ability. Taking the rotation of the torso around the x axis (the change of roll joint) as an example, the following constraints are used

$$\theta_{\min}^{x} \leq \boldsymbol{S}_i\boldsymbol{P}_{pu}\boldsymbol{S}_\theta^{x}\boldsymbol{u}_k + \boldsymbol{S}_i\boldsymbol{P}_{ps}\hat{\boldsymbol{\theta}}_k^{x} \leq \theta_{\max}^{x}, i \in \{1, \ldots, N_h\}, \tag{41}$$

$$\tau_{\min}^{x} \leq J_x\left(\boldsymbol{S}_i\boldsymbol{P}_{au}\boldsymbol{S}_\theta^{x}\boldsymbol{u}_k + \boldsymbol{S}_i\boldsymbol{P}_{as}\hat{\boldsymbol{\theta}}_k^{x}\right) \leq \tau_{\min}^{x}, i \in \{1, \ldots, N_h\}, \tag{42}$$

where $\theta_{\min}^{x}$ and $\theta_{\max}^{x}$ are minimum and maximum values of roll angle, respectively, $\tau_{\min}^{x}$ and $\tau_{\max}^{x}$ are the minimum and maximum torques of the roll joint, respectively.
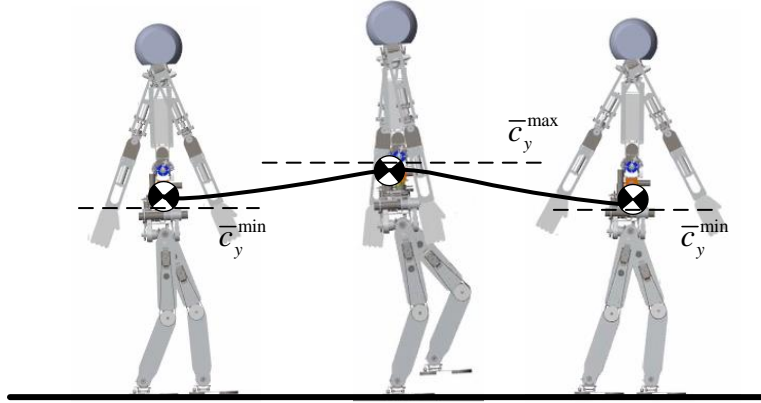
11

Figure 5: Changes in the height of CoM during walking. The height of the robot's CoM reaches the maximum in the single support phase and the minimum in the double support phase.

3.4. Optimization for walk

3.4.1. SQP for linearization of QCQP

Once the QCQP in (25) is generated, it can be transformed to a SQP. The SQP we used here is quite simple. The SQP linearizes the QCQP around the initial iteration point [44]

$$
\min_{\delta} \frac{1}{2} \boldsymbol{\delta}^{\mathrm{T}} \nabla^2_{\boldsymbol{u}_k} \left(\psi \left(\boldsymbol{u}_k \right) \right) \boldsymbol{\delta} + \left(\nabla_{\boldsymbol{u}_k} \psi \left(\boldsymbol{u}_k \right) \right)^{\mathrm{T}} \boldsymbol{\delta}
$$

$$
\text{s.t}
$$

$$
\left(\nabla_{\boldsymbol{u}_k} h_i \left(\boldsymbol{u}_k \right) \right)^{\mathrm{T}} \boldsymbol{\delta} + h_i \left(\boldsymbol{u}_k \right) \leq 0,
$$

$$
i \in \{1, \ldots, N_h\} .
$$

(43)

As a result, we can obtain a QP, and it can be solved easily via QP solver.

3.4.2. Optimal CoM height for walk

We note that the CoM height seems to be held on a constant value with the optimization of (25) since the optimization always tries to minimize the jerks. It was found through experiments that the trajectory of the centroid height of human walking was approximately a sine function [45, 46]. The height of the CoM reaches the highest point in the single support phase and decreases to the minimum value in the double support phase. For simplification, we only set the reference CoM height in the single and double support phases, $\bar{c}_y^{\max}$ and $\bar{c}_y^{\min}$, to constant values by trial and error, as shown in Fig. 5.

Figure 6 shows the detailed block diagram of our proposed method. Inputs to the planner are the actual and reference CoM height, torso rotation angles and footholds. As a result, the proposed framework can find a reliable solution for the robot to perform some given tasks. With the optimized CoM trajectory, torso rotational angle and footholds, a singularity-tolerant inverse kinematics solver [47] is used to compute the joint trajectories.

4. Simulations

In this section, different scenarios are produced to evaluate the proposed NMPC applied to the FCDIP. All the simulations are finished in Matlab/Simcape.

4.1. Modeling reality

The humanoid robot is developed and currently under construction in the Bionic Robotics Laboratory at SEU, supported by the National Natural Science Foundation of China. The robot's height is about 1.34 m (not including
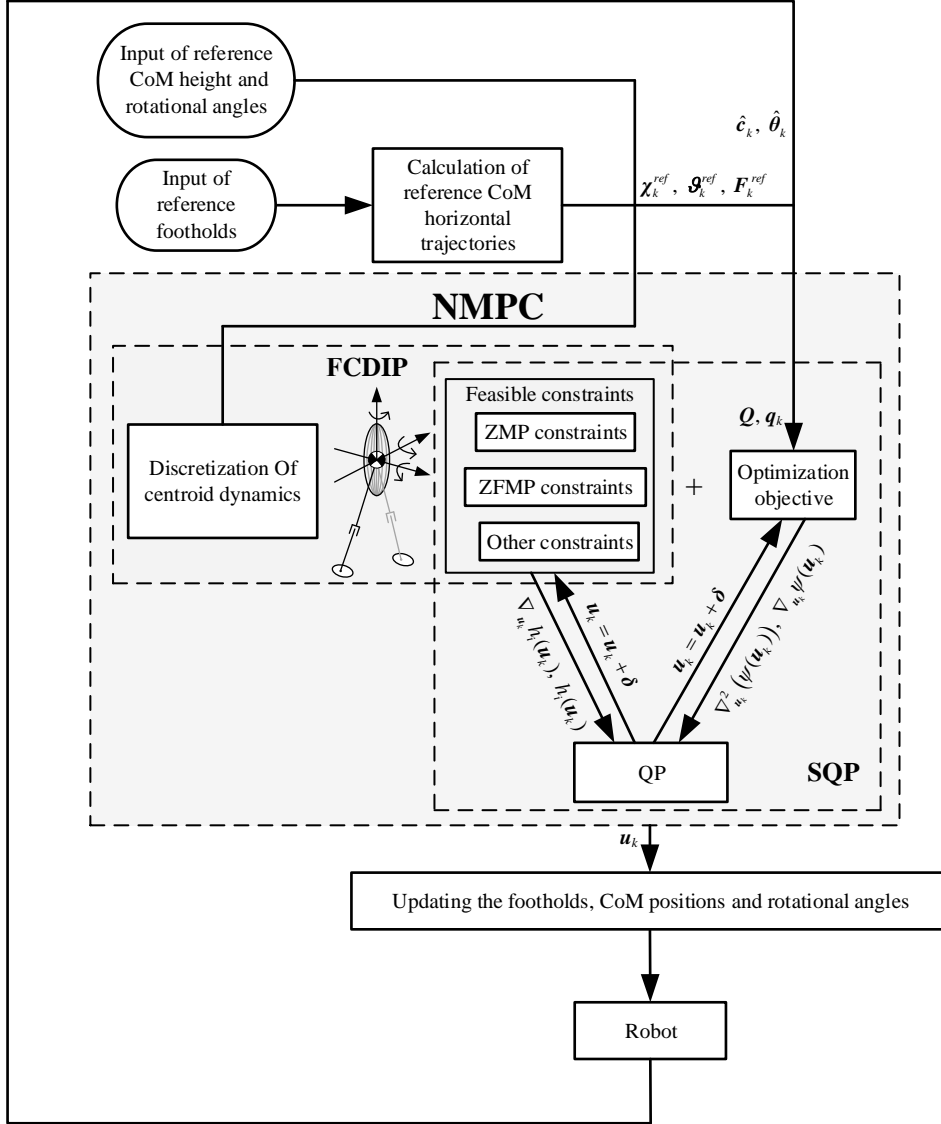
Figure 6: Planner block diagram. The blocks in the shaded area in the center of the figure applies to NMPC which consists of the abstract model, FCDIP, and the SQP. After inputting the reference CoM height, rotational angles and foothold, the QCQP can be obtained with the discretization of centroid dynamics. Next, the SQP approach linearizes the QCQP such that it would be a QP, the solution of QP, $\boldsymbol{\delta}$, is then used to update the input, $\boldsymbol{u}_k$, via $\boldsymbol{u}_k = \boldsymbol{u}_k + \boldsymbol{\delta}$. Then, the footholds, CoM positions and rotational angles are updated via (22) and (23) with a timestep. Finally, the whole procedure is repeated to generate the future trajectory.

Table 1: Physical parameters of the robot.

Limb	Mass /kg	Inertia (simplification) /kg.m^2	Size/m
Foot	0.214	$[65.054\ 0\ 0; 0\ 793.176\ 0; 0\ 0\ 730.63] \times 10^{-6}$	Length:0.22 Width:0.16 Height: 0.051
Shank	1.385	$[13906.193\ 0\ 0; 0\ 1797.345\ 0; 0\ 0\ 13374.942] \times 10^{-6}$	0.282
Thigh	3.305	$[30502.901\ 0\ 0\ ; 0\ 5065.5470\ ; 0\ 0\ 27530.223] \times 10^{-6}$	0.35
Pelvis	9.912	$[30517.03\ 0\ 0\ ; 0\ 48884.036\ 0\ ; 0\ 0\ 6285.625] \times 10^{-6}$	0.333
Waist	5.019	$[45714.741\ 0\ 0\ ; 0\ 7616.767\ 0\ ; 0\ 0\ 46090.578] \times 10^{-6}$	0.133
Torso	8.907	$[52532.919\ 0\ 0; 0\ 21641.936\ 0; 0\ 0\ 40705.475] \times 10^{-6}$	0.391
Scapula	0.312	$[2378.86\ 0\ 0; 0\ 2457.132\ 0; 0\ 0\ 181.043] \times 10^{-6}$	0.447
Arm	3.447	$[165613.583\ 0\ 0; 0\ 7700.712\ 0; 0\ 0\ 160759.296] \times 10^{-6}$	0.605

the head), and its mass is about 40 kg. It is designed to have a full-sized body with 23 deg. Herein, we will fix some joints appropriately as needed. Table 1 provides the physical parameters which are derived from SolidWorks. In the simulation, the robot joints are position-servo-controlled to track the trajectories generated by the NMPC and inverse kinematics algorithm. The sampling time of the simulation is 0.0001s. The CoM is assumed to be set at the waist of the robot. Besides, the walking surface is modelled as a nonlinear spring-damper system [48].

4.2. Case.1 Steering from the straight walking

To test the the effects of the proposed ZFMP, in the first set of experiments, the robot steers from straight walking. Firstly, the robot begins to walk from standing still. The robot performs 10° turning in each step while steering. The reference walking period and stride length are 0.5 s (20% for the double support phase) and 0.25 m, respectively. The torso is expected to keep upright for stabilization; thus, the reference torso rotation angles are all set to zero. Besides, the motion of the arm is described by a sinusoidal timing law characterised by the same frequency of the gait. This choice has been made based on trials carried out to counteract the swing dynamics of the leg. The modulation is visible in Video 1.

(a) CoM height

(b) Walking speed

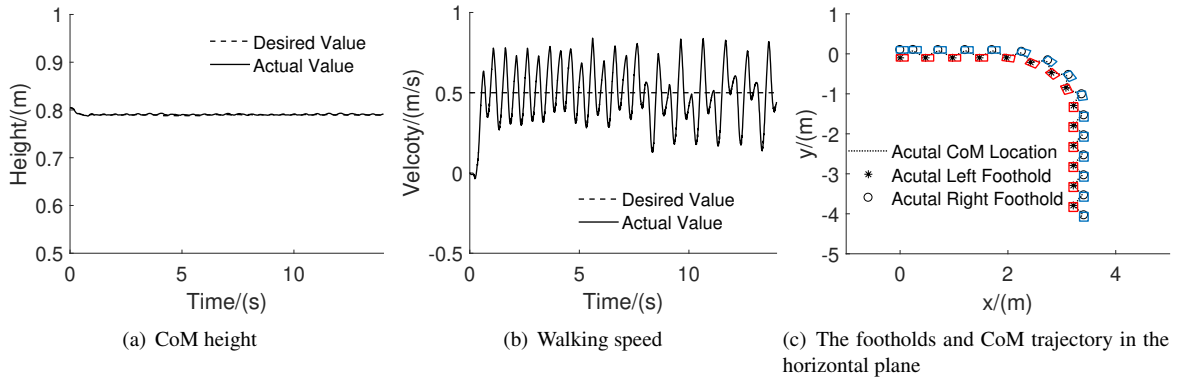(c) The footholds and CoM trajectory in the horizontal plane

Figure 7: The motion of the robot steers from straight walking.

The results are shown in Figs. 7-9. Figure 7(a) shows that the height of the CoM fluctuates around the desired value. Besides, the robot can quickly reach the desired average speed, as shown in Fig. 7 (b). Figure 7 (c) records the position of the robot's foothold and the trajectory of its CoM. Empirically, it has been found that the path of a human's CoM while walking resembles a parabola [49]. The result also shows that the CoM moves back and forth like a parabola between the left and right feet. In Fig. 8, the measured GRFs indicate there are larger landing impacts during steering, which may be the reason that the ZFMP is sometimes not inside the support polygon (see Fig. 9). The ZFMP is only outside the theoretical bounds for a few moments, not an extended period; therefore, there is no significant rotational slippage on the feet. Here, it should be noted that the upper and lower boundaries of the ZFMP are determined only by the geometry of the support polygon in the single support phase.
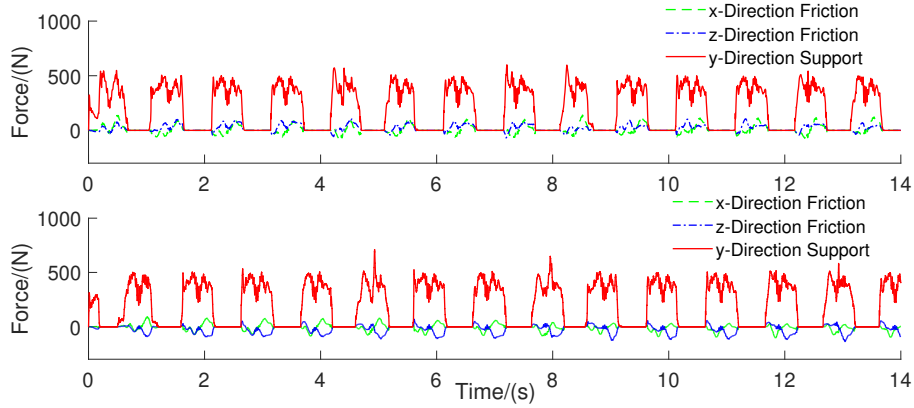
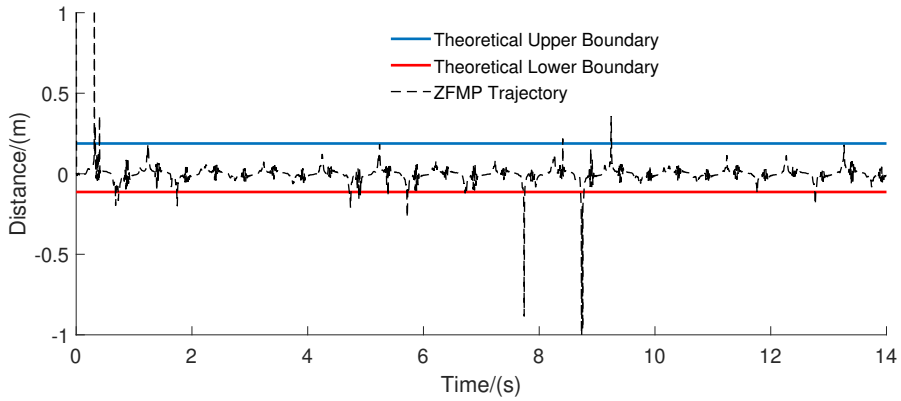Figure 8: GRFs during walking (top: left foot, bottom: right foot).

Figure 9: ZFMP during the walking.

To further reflect the necessity of our ZFMP in steering, we input an extreme reference trajectory, turning 90° in a single step. Next, the robot is tested with and without the ZFMP constraints. As shown in Fig. 10, due to the ZFMP constraints, the robot cannot execute a 90-degree turn in a single step. During a steering, a significant yaw moment is eliminated to prevent the ZFMP from moving outside the support polygon. Therefore, the robot must navigate a 90-degree turn by executing several small-angle turns.(see Fig. 10(a)). Conversely, not enforcing the ZFMP constraint may cause instability and even falling, as shown in Figs 10 and 11. Figure 10(c) shows that the hip yaw torque is limited between about −20 Nm and 20 Nm with ZFMP constraint while the hip yaw torque is much higher without ZFMP constraint. In Fig. 10(a), the dotted line is the foot location after its rotation. Figure 11 shows the time instant when rotation and sliding occur. The results indicate the importance of the ZFMP constraint during sharp turning. Note that, if the dynamics of yaw motion and ZFMP are not considered, FCDIP degenerates into something similar to VIP[23] and NIPF[24]. Thus, the steering test with or without ZFMP can also be seen as a contrast between FCDIP and VIP as well as NIPF. The results indicate that considering yaw dynamics and ZFMP is what makes FCDIP an advanced version of VIP and NIPF.

4.3. Case.2 Walking underneath a low door

Walking with variable CoM height enhances the robot's flexibility and enables it to perform a wider range of tasks.The second experiment considers the robot crossing underneath a door whose top frame is low. Here, we assume the location and height of the door are known relative to that of the robot; therefore, the reference footholds and postures are also given in advance. The robot lowers its CoM by about 0.1 m and bends its torso forward by 60° while crossing the low door. After passing the door, the robot returns to its original CoM height and upper posture.

Figure 12 shows the snapshots of the experimental results. The humanoid robot can successfully pass a low door. as shown in Figs. 13-15. We observe that the robot can track the desired optimized trajectory well with an average speed of 0.5 m/s. Figures 13 (c, d) show that the robot bends its torso to pass the door between 4 s and 6 s. Figure 13 (d) also exhibits the orientation of the torso while the robot walks upright, which is probably influenced by the dynamics of walking, e.g., the swing and landing of the legs. The phenomenon is supported by the GRF as shown in Fig. 14. The support force increases rapidly when the foot lands on the ground. Ideally, the sum of support forces should be roughly the same as the gravitation force; however, they differ due to the swing dynamics. Figure. 15 shows the feet's positions and ZMP trajectory. The ZMP trajectory always stays close to the feet positions and generally inside the support polygon. Sometimes the ZMP reaches the edge of the support polygon due to landing impact.

Walking with the variable CoM height also has another merit. Figure. 16 illustrates the integral of the joint torque required when the robot takes one step with constant and variable CoM height at different walking speeds. We refer to the integral of the required joint torque as the sthenic criterion. In this case, the walking period is 0.5 s. Furthermore, the CoM height is set to 0.76 m while walking without CoM height changes, and the highest and lowest CoM heights for variable-height walking are 0.81 m and 0.75 m, respectively. The sthenic criterion C of the robot each joint is obtained as[1]

$$C = \int_0^T \tau^2 dt, \tag{44}$$

where T are the action duration of the joints, respectively. τ is the joint torque. Figure. 16 shows that it is evident that the sthenic criterion of walking with variable CoM height is less than that of walking with constant CoM height. The robot can reduce about 20% energy consumption per meter with variable CoM height. Besides, we can also observe that the difference in the total energy consumption between the two situations is similar to that in the knee. In other words, the knee is the critical joint that accounts for this phenomenon. The knee needs more power to support the upper body if the robot stretches its legs, which is understandable. Thus, our proposed method copes with tasks in complex environments and generates a more natural gait.

Moreover, the robot could perform more tasks if the DoF of the CoM height is free. Figure. 17 shows the robot's locomotion going upstairs using our proposed method. In this case, the height and length of the stairs are 0.2 m and 0.25 m, respectively.

4.4. Case.3 Push recovery during walking

In this case, the robustness of our proposed method is tested by suddenly applying horizontal external forces those at the torso (1.2m) during walking. In [24] and [50], push recovery via reactive step strategy and angular momentum strategy (also called hip strategy) was analyzed. Similarly, in this section, benefiting from FCDIP supporting six-dimensional motion, the rotation of the torso and stride adjustment could be utilized for maintaining balance. As a comparison, we also tested the robustness of LIP and VHIP. We conduct repeated tests with push magnitudes of 150N and 250N, each lasting 0.1s. The push recovery results under different external forces are demonstrated in Fig. 18 and Fig. 19.

As depicted in Fig. 18, whether utilizing LIP, VHIP, or FCDIP, the robot could preserve balance amid external interference by adjusting the landing foothold. The distinction lies in the fact that, with FCDIP, the robot exhibits a shorter reaction step length due to the active bending of the torso (see Figs. 19 (a) and (b)). Actively adjusting the angular momentum of the robot can enhance the robot's anti-interference ability [24, 51]. In this scenario, to enlarge the stride length for maintaining balance under the forward push, the robot needs to slightly adjust its height to attain a reachable foothold as shown in Figs. 19 (c) and (d). For LIP, it cannot change its height, thus, it should always bend its knees for the event of needing to take a large stride. As mentioned earlier, walking with constantly bent knees is not only unnatural but also more energy-consuming. As depicted in Fig. 19 (d), the minimum CoM height with FCDIP is the lowest among the three strategies as a result of stooping. FCDIP supports the rotating motion of the torso, and the bending motion results in reducing the robot's CoM height. It is also interesting to notice that there is no significant difference in the ability to resist external interference between LIP and VHIP as shown in Table. 2. Even

---

[1]In this study, we do not choose the cost of transport or mechanical work as an evaluation criterion for joints. Instead, the time integral of the joint torques is chose to evaluate the energy consumption. This is because the torque output is connected to the current, which is directly associated with the actual electric power consumption.

Table 2: Robot's ability to maintaining balance from the forward pushes with different action duration.

Model	LIP	VHIP	FCDIP
0.1s	305N	315N	340N
0.2s	210N	205N	235N
0.3s	160N	145N	180N

with a prolonged duration of external force application, the anti-external force capability of using VHIP weakens. When using LIP, the CoM is lower, resulting in minimized heavy and external moments. Moreover, whether VHIP or FCDIP is employed, the knee joint approaches singularity, i.e., the straight leg, resulting in strong vertical bearing capacity and poor horizontal support capacity [52]. The strong vertical bearing capacity is also consistent with the low energy consumption of our straight-leg walking.

5. Discussion and conclusion

This work demonstrates how to generate biped locomotion for humanoid robots walking in complicated environments. The complex mechanism and nonlinear dynamics of the robot brought many problems. Motivated to solve these practical issues, we introduced a new 3D simplified model with more DoFs. Compared to other simplified models, the proposed model considered vertical and yaw dynamics. The variable CoM height affected the ZMP dynamics, thus, trajectory planning using ZMP was a classical nonlinear problem. This issue was skillfully expressed as a QCQP in closed form. Thanks to the SQP, this closed-form formulation could find the gradients and Hessian of the QCQP numerically to solve the QCQP. Besides, we also introduced a new stability criterion named ZFMP for robot steering. Using only the ZMP information, one cannot determine whether the sole is slipping on the ground surface as the ZMP represents two-dimensional information about the GRF. Determining the transition of contact states requires six-dimensional information about the force/moment. Here, we considered adopting the full-dimensional force/moment corresponding to FCDIP. The ZFMP is similar to the ZMP and should be within the support polygon to ensure a stable turn. To the best of our knowledge, no similar criteria have been proposed to evaluate the stability of turning. To demonstrate the efficiency of our proposed method, we simulate various aperiodic locomotion scenarios, including walking underneath a low door, steering, and recovering from a push. These results showed that the proposed method can automatically generate the CoM trajectory, torso rotational angle and foot placement positions for robot walking in complex environments. In addition, we also noticed that walking with variable CoM height can slightly reduce the energy consumption for walking.

Although the proposed method can handle various walking environments and tasks, it still lacks of some natural locomotion behaviors, e.g., heel-strike and toe-off motion. Therefore, our future work will continue to investigate more natural biped walking.

Appendix A.

The coefficient matrices $P_{ps}, P_{pu}, P_{vs}, P_{vu}, P_{as}$ and P_{au} can be calculated by iteration of (16). Here, we take P_{ps} and P_{pu} as examples

17

$$\boldsymbol{P}_{ps} = \begin{bmatrix} \boldsymbol{c}_p\boldsymbol{A}, & \boldsymbol{c}_p\boldsymbol{A}^2, & \cdots, & \boldsymbol{c}_p\boldsymbol{A}^{N_h} \end{bmatrix}^{\mathrm{T}} = \begin{bmatrix} 1 & T & T^2/2 \\ 1 & 2T & 2T^2 \\ \vdots & \vdots & \vdots \\ 1 & N_hT & N_h^2T^2/2 \end{bmatrix}, \tag{A.1}$$

$$\boldsymbol{P}_{pu} = \begin{bmatrix} \boldsymbol{c}_p\boldsymbol{B} & 0 & \cdots & 0 \\ \boldsymbol{c}_p\boldsymbol{A}^1\boldsymbol{B} & \boldsymbol{c}_p\boldsymbol{B} & \cdots & 0 \\ \vdots & \vdots & \ddots & 0 \\ \boldsymbol{c}_p\boldsymbol{A}^{N_h-1}\boldsymbol{B} & \boldsymbol{c}_p\boldsymbol{A}^{N_h-2}\boldsymbol{B} & \cdots & \boldsymbol{c}_p\boldsymbol{B} \end{bmatrix}$$

$$= \begin{bmatrix} T^3/6 & 0 & \cdots & 0 \\ 7T^3/6 & T^3/6 & \cdots & 0 \\ \vdots & \vdots & \ddots & 0 \\ \left(3N_h^2 - 3N_h + 1\right)T^3/6 & \left(3\left(N_h - 1\right)^2 - 3\left(N_h - 1\right) + 1\right)T^3/6 & \cdots & T^3/6 \end{bmatrix}, \tag{A.2}$$

where $\boldsymbol{c}_p = \begin{bmatrix} 1 & 0 & 0 \end{bmatrix}$ represent the selection matrix to extract the position component from the centroid condition vector. Similarly, the $\boldsymbol{P}_{vs}, \boldsymbol{P}_{vu}, \boldsymbol{P}_{as}$ and $\boldsymbol{P}_{au}$ can be obtained by replacing $\boldsymbol{c}_p$ with $\boldsymbol{c}_v = \begin{bmatrix} 0 & 1 & 0 \end{bmatrix}$ and $\boldsymbol{c}_a = \begin{bmatrix} 0 & 0 & 1 \end{bmatrix}$, respectively.

$$\boldsymbol{P}_{vs} = \begin{bmatrix} 0 & 1 & T \\ 0 & 1 & 2T \\ \vdots & \vdots & \vdots \\ 0 & 1 & NT \end{bmatrix}, \tag{A.3}$$

$$\boldsymbol{P}_{vu} = \begin{bmatrix} T^2/2 & 0 & \cdots & 0 \\ 3T^2/2 & T^2/2 & \cdots & 0 \\ \vdots & \vdots & \ddots & 0 \\ (2N - 1)T^2/2 & (2(N - 1) - 1)T^2/2 & \cdots & T^2/2 \end{bmatrix}, \tag{A.4}$$

$$\boldsymbol{P}_{as} = \begin{bmatrix} 0 & 0 & 1 \\ \vdots & \vdots & \vdots \\ 0 & 0 & 1 \end{bmatrix}, \tag{A.5}$$

$$\boldsymbol{P}_{au} = \begin{bmatrix} T & 0 & 0 \\ \vdots & \ddots & 0 \\ T & \cdots & T \end{bmatrix}. \tag{A.6}$$

Appendix B.

Here, we consider the optimization problem in x-direction as an example. Substituting (18)-(23) into equation (24) and eliminating the selection matrix S_i, we obtain

$$\min_{u_k} \frac{\alpha_p}{2}\left(\boldsymbol{P}_{ps}\hat{\boldsymbol{c}}_k^x + \boldsymbol{P}_{pu}\boldsymbol{S}_j^x\boldsymbol{u}_k - \bar{\boldsymbol{c}}_k^x\right)^{\mathrm{T}}\left(\boldsymbol{P}_{ps}\hat{\boldsymbol{c}}_k^x + \boldsymbol{P}_{pu}\boldsymbol{S}_j^x\boldsymbol{u}_k - \bar{\boldsymbol{c}}_k^x\right) + \frac{\alpha_v}{2}\left(\boldsymbol{P}_{vs}\hat{\boldsymbol{c}}_k^x + \boldsymbol{P}_{vu}\boldsymbol{S}_j^x\boldsymbol{u}_k\right)^{\mathrm{T}}\left(\boldsymbol{P}_{vs}\hat{\boldsymbol{c}}_k^x + \boldsymbol{P}_{vu}\boldsymbol{S}_j^x\boldsymbol{u}_k\right)$$

$$+ \frac{\alpha_j}{2}\left(\boldsymbol{S}_j^x\boldsymbol{u}_k\right)^{\mathrm{T}}\boldsymbol{S}_j^x\boldsymbol{u}_k + \frac{\beta_p}{2}\left(\boldsymbol{P}_{ps}\hat{\boldsymbol{\theta}}_k^x + \boldsymbol{P}_{pu}\boldsymbol{S}_\theta^x\boldsymbol{u}_k - \boldsymbol{\theta}_k^x\right)^{\mathrm{T}}\left(\boldsymbol{P}_{ps}\hat{\boldsymbol{\theta}}_k^x + \boldsymbol{P}_{pu}\boldsymbol{S}_\theta^x\boldsymbol{u}_k - \boldsymbol{\theta}_k^x\right) \tag{B.1}$$

$$+ \frac{\beta_v}{2}\left(\boldsymbol{P}_{vs}\hat{\boldsymbol{\theta}}_k^x + \boldsymbol{P}_{vu}\boldsymbol{S}_\theta^x\boldsymbol{u}_k\right)^{\mathrm{T}}\left(\boldsymbol{P}_{vs}\hat{\boldsymbol{\theta}}_k^x + \boldsymbol{P}_{vu}\boldsymbol{S}_\theta^x\boldsymbol{u}_k\right) + \frac{\beta_j}{2}\left(\boldsymbol{S}_\theta^x\boldsymbol{u}_k\right)^{\mathrm{T}}\boldsymbol{S}_\theta^x\boldsymbol{u}_k + \frac{\gamma}{2}\left(\boldsymbol{S}_f^x\boldsymbol{u}_k - \bar{\boldsymbol{f}}_k^x\right)^{\mathrm{T}}\left(\boldsymbol{S}_f^x\boldsymbol{u}_k - \bar{\boldsymbol{f}}_k^x\right).$$

Next, we take the position states, i.e., the first three terms of (B.1), as an example and expand them

$$
\begin{aligned}
& \frac{\alpha_p}{2}\left(\left(\hat{c}_k^x\right)^{\mathrm T} \boldsymbol P_{ps}^{\mathrm T} \boldsymbol P_{ps}\hat{c}_k^x + \left(\hat{c}_k^x\right)^{\mathrm T} \boldsymbol P_{ps}^{\mathrm T} \boldsymbol P_{pu}\boldsymbol S_j^x \boldsymbol u_k - \left(\hat{c}_k^x\right)^{\mathrm T} \boldsymbol P_{ps}^{\mathrm T} \overline{c}_k^x + \boldsymbol u_k^{\mathrm T}\left(\boldsymbol S_j^x\right)^{\mathrm T} \boldsymbol P_{pu}^{\mathrm T} \boldsymbol P_{ps}\hat{c}_k^x + \boldsymbol u_k^{\mathrm T}\left(\boldsymbol S_j^x\right)^{\mathrm T} \boldsymbol P_{pu}^{\mathrm T} \boldsymbol P_{pu}\boldsymbol S_j^x \boldsymbol u_k\right) \\
& + \frac{\alpha_p}{2}\left(-\boldsymbol u_k^{\mathrm T}\left(\boldsymbol S_j^x\right)^{\mathrm T} \boldsymbol P_{pu}^{\mathrm T} \overline{c}_k^x - \left(\overline{c}_k^x\right)^{\mathrm T} \boldsymbol P_{ps}\hat{c}_k^x - \left(\overline{c}_k^x\right)^{\mathrm T} \boldsymbol P_{pu}\boldsymbol S_j^x \boldsymbol u_k + \left(\overline{c}_k^x\right)^{\mathrm T} \overline{c}_k^x\right) \qquad \text{(B.2)}\\
& + \frac{\alpha_v}{2}\left(\left(\hat{c}_k^x\right)^{\mathrm T} \boldsymbol P_{vs}^{\mathrm T} \boldsymbol P_{vs}\hat{c}_k^x + \left(\hat{c}_k^x\right)^{\mathrm T} \boldsymbol P_{vs}^{\mathrm T} \boldsymbol P_{vu}\boldsymbol S_j^x \boldsymbol u_k + \boldsymbol u_k^{\mathrm T}\left(\boldsymbol S_j^x\right)^{\mathrm T} \boldsymbol P_{vu}^{\mathrm T} \boldsymbol P_{vs}\hat{c}_k^x + \boldsymbol u_k^{\mathrm T}\left(\boldsymbol S_j^x\right)^{\mathrm T} \boldsymbol P_{vu}^{\mathrm T} \boldsymbol P_{vu}\boldsymbol S_j^x \boldsymbol u_k\right) + \frac{\alpha_j}{2}\boldsymbol u_k^{\mathrm T}\left(\boldsymbol S_j^x\right)^{\mathrm T} \boldsymbol S_j^x \boldsymbol u_k.
\end{aligned}
$$

Here, these terms $\left(\hat{c}_k^x\right)^{\mathrm T} \boldsymbol P_{ps}^{\mathrm T} \boldsymbol P_{ps}\hat{c}_k^x, -\left(\hat{c}_k^x\right)^{\mathrm T} \boldsymbol P_{ps}^{\mathrm T} \overline{x}_k^x, -\left(\overline{c}_k^x\right)^{\mathrm T} \boldsymbol P_{ps}\hat{c}_k^x, \left(\overline{c}_k^x\right)^{\mathrm T} \overline{c}_k^x$, and $\left(\hat{c}_k^x\right)^{\mathrm T} \boldsymbol P_{vs}^{\mathrm T} \boldsymbol P_{vs}\hat{c}_k^x$ are constants. Therefore, they are not involved in the optimization process and can be removed. Then (B.2) becomes

$$
\begin{aligned}
& \frac{\alpha_p}{2}\left(\boldsymbol u_k^{\mathrm T}\left(\boldsymbol S_j^x\right)^{\mathrm T} \boldsymbol P_{pu}^{\mathrm T} \boldsymbol P_{pu}\boldsymbol S_j^x \boldsymbol u_k + (\hat{c}_k^x)^{\mathrm T} \boldsymbol P_{ps}^{\mathrm T} \boldsymbol P_{pu}\boldsymbol S_j^x \boldsymbol u_k + \boldsymbol u_k^{\mathrm T}\left(\boldsymbol S_j^x\right)^{\mathrm T} \boldsymbol P_{pu}^{\mathrm T} \boldsymbol P_{ps}\hat{c}_k^x - \boldsymbol u_k^{\mathrm T}\left(\boldsymbol S_j^x\right)^{\mathrm T} \boldsymbol P_{pu}^{\mathrm T} \overline{c}_k^x - \left(\overline{c}_k^x\right)^{\mathrm T} \boldsymbol P_{pu}\boldsymbol S_j^x \boldsymbol u_k\right) \\
& + \frac{\alpha_v}{2}\left(\boldsymbol u_k^{\mathrm T}\left(\boldsymbol S_j^x\right)^{\mathrm T} \boldsymbol P_{vu}^{\mathrm T} \boldsymbol P_{vu}\boldsymbol S_j^x \boldsymbol u_k + (\hat{c}_k^x)^{\mathrm T} \boldsymbol P_{vs}^{\mathrm T} \boldsymbol P_{vu}\boldsymbol S_j^x \boldsymbol u_k + \boldsymbol u_k^{\mathrm T}\left(\boldsymbol S_j^x\right)^{\mathrm T} \boldsymbol P_{vu}^{\mathrm T} \boldsymbol P_{vs}\hat{c}_k^x\right) + \frac{\alpha_j}{2}\boldsymbol u_k^{\mathrm T}\left(\boldsymbol S_j^x\right)^{\mathrm T} \boldsymbol S_j^x \boldsymbol u_k.
\end{aligned}
\qquad \text{(B.3)}
$$

Note that, $(\hat{c}_k^x)^{\mathrm T} \boldsymbol P_{ps}^{\mathrm T} \boldsymbol P_{pu}\boldsymbol S_j^x \boldsymbol u_k$ and $\boldsymbol u_k^{\mathrm T}\left(\boldsymbol S_j^x\right)^{\mathrm T} \boldsymbol P_{pu}^{\mathrm T} \boldsymbol P_{ps}\hat{c}_k^x$ are the same terms. Similarly, $-\boldsymbol u_k^{\mathrm T}\left(\boldsymbol S_j^x\right)^{\mathrm T} \boldsymbol P_{pu}^{\mathrm T} \overline{c}_k^x$ and $-\left(\overline{c}_k^x\right)^{\mathrm T} \boldsymbol P_{pu}\boldsymbol S_j^x \boldsymbol u_k$, $(\hat{c}_k^x)^{\mathrm T} \boldsymbol P_{vs}^{\mathrm T} \boldsymbol P_{vu}\boldsymbol S_j^x \boldsymbol u_k$ and $\boldsymbol u_k^{\mathrm T}\left(\boldsymbol S_j^x\right)^{\mathrm T} \boldsymbol P_{vu}^{\mathrm T} \boldsymbol P_{vs}\hat{c}_k^x$ also represent identical terms. Hence, (B.3) simplifies as follows

$$
\begin{aligned}
& \left(\frac{\alpha_p}{2}\boldsymbol u_k^{\mathrm T}\left(\boldsymbol S_j^x\right)^{\mathrm T} \boldsymbol P_{pu}^{\mathrm T} \boldsymbol P_{pu}\boldsymbol S_j^x \boldsymbol u_k + \frac{\alpha_v}{2}\boldsymbol u_k^{\mathrm T}\left(\boldsymbol S_j^x\right)^{\mathrm T} \boldsymbol P_{vu}^{\mathrm T} \boldsymbol P_{vu}\boldsymbol S_j^x \boldsymbol u_k + \frac{\alpha_j}{2}\boldsymbol u_k^{\mathrm T}\left(\boldsymbol S_j^x\right)^{\mathrm T} \boldsymbol S_j^x \boldsymbol u_k\right) \\
& + \left(\alpha_p(\hat{c}_k^x)^{\mathrm T} \boldsymbol P_{ps}^{\mathrm T} \boldsymbol P_{pu}\boldsymbol S_j^x \boldsymbol u_k + \alpha_v(\hat{c}_k^x)^{\mathrm T} \boldsymbol P_{vs}^{\mathrm T} \boldsymbol P_{vu}\boldsymbol S_j^x \boldsymbol u_k - \alpha_p\left(\overline{c}_k^x\right)^{\mathrm T} \boldsymbol P_{pu}\boldsymbol S_j^x \boldsymbol u_k\right).
\end{aligned}
\qquad \text{(B.4)}
$$

Finally, let's tidy up the (B.4) and transform it into

$$
\boldsymbol u_k^T
\begin{bmatrix}
\frac{\alpha_j}{2}\boldsymbol I^{N_h \times N_h} + \frac{\alpha_v}{2}\boldsymbol P_{vu}^{\mathrm T} \boldsymbol P_{vu} + \frac{\alpha_p}{2}\boldsymbol P_{pu}^{\mathrm T} \boldsymbol P_{pu} & \boldsymbol 0 & \cdots & \boldsymbol 0 \\
\boldsymbol 0 & \square & \boldsymbol 0 & \boldsymbol 0 \\
\vdots & \vdots & \ddots & \vdots \\
\boldsymbol 0 & \boldsymbol 0 & \boldsymbol 0 & \square
\end{bmatrix}
\boldsymbol u_k +
\begin{bmatrix}
\alpha_p \boldsymbol P_{pu}^{\mathrm T} \boldsymbol P_{ps}\hat{c}_k^x + \alpha_v \boldsymbol P_{vu}^{\mathrm T} \boldsymbol P_{vs}\hat{c}_k^x - \alpha_p \boldsymbol P_{pu}^{\mathrm T} \overline{c}_k^x \\
\square \\
\vdots \\
\square
\end{bmatrix}^{\mathrm T}
\boldsymbol u_k, \quad \text{(B.5)}
$$

where $\boldsymbol Q = \begin{bmatrix}
\frac{\alpha_j}{2}\boldsymbol I^{N_h \times N_h} + \frac{\alpha_v}{2}\boldsymbol P_{vu}^{\mathrm T} \boldsymbol P_{vu} + \frac{\alpha_p}{2}\boldsymbol P_{pu}^{\mathrm T} \boldsymbol P_{pu} & \boldsymbol 0 & \cdots & \boldsymbol 0 \\
\boldsymbol 0 & \square & \boldsymbol 0 & \boldsymbol 0 \\
\vdots & \vdots & \ddots & \vdots \\
\boldsymbol 0 & \boldsymbol 0 & \boldsymbol 0 & \square
\end{bmatrix}$ and $\boldsymbol q_k = \begin{bmatrix}
\alpha_p \boldsymbol P_{pu}^{\mathrm T} \boldsymbol P_{ps}\hat{c}_k^x + \alpha_v \boldsymbol P_{vu}^{\mathrm T} \boldsymbol P_{vs}\hat{c}_k^x - \alpha_p \boldsymbol P_{pu}^{\mathrm T} \overline{c}_k^x \\
\square \\
\vdots \\
\square
\end{bmatrix}$.

The terms represented by the remaining squares in (B.5), namely, the optimization matrices or vectors of the position states in the *y*-direction, the *z*-direction, the rotation of the CoM, and the footholds can be obtained in a similar manner.

References

[1] S. Kajita, H. Hirukawa, K. Harada, K. Yokoi, Introduction to humanoid robotics, Springer, 2014.

[2] S. Faraji, A. J. Ijspeert, 3lp: A linear 3d-walking model including torso and swing dynamics, The International Journal of Robotics Research 36 (4) (2017) 436–455.

[3] Z. Xie, L. Li, X. Luo, Three-dimensional aperiodic biped walking including the double support phase using lipm and lpm, Robotics and Autonomous Systems 143 (2021) 103831.

[4] S. E. Ada, E. Ugur, H. L. Akin, Generalization in transfer learning: robust control of robot locomotion, Robotica 40 (11) (2022) 3811–3836.

[5] J. Englsberger, Combining reduced dynamics models and whole-body control for agile humanoid locomotion, Ph.D. thesis, Technische Universität München (2016).

[6] M. Johnson, B. Shrewsbury, S. Bertrand, T. Wu, D. Duran, M. Floyd, P. Abeles, D. Stephen, N. Mertins, A. Lesman, et al., Team ihmc's lessons learned from the darpa robotics challenge trials, Journal of Field Robotics 32 (2) (2015) 192–208.

[7] H. Herr, M. Popovic, Angular momentum in human walking, Journal of experimental biology 211 (4) (2008) 467–481.

[8] J. Ding, L. Han, L. Ge, Y. Liu, J. Pang, Robust locomotion exploiting multiple balance strategies: an observer-based cascaded model predictive control approach, IEEE/ASME Transactions on Mechatronics 27 (4) (2022) 2089–2097.

[9] T. McGeer, Passive dynamic walking, The International Journal of Robotics Research 9 (2) (1990) 62–82.

[10] X. Luo, W. Xu, Planning and control for passive dynamics based walking of 3d biped robots, Journal of Bionic Engineering 9 (2) (2012) 143–155.

[11] X. Luo, L. Zhu, L. Xia, Principle and method of speed control for dynamic walking biped robots, Robotics and Autonomous Systems 66 (2015) 129–144.

[12] X. Luo, D. Xia, C. Zhu, Impact dynamics-based torso control for dynamic walking biped robots, International Journal of Humanoid Robotics 15 (03) (2018) 1850004.

[13] S. Kajita, F. Kanehiro, K. Kaneko, K. Fujiwara, K. Harada, K. Yokoi, H. Hirukawa, Biped walking pattern generation by using preview control of zero-moment point, in: 2003 IEEE International Conference on Robotics and Automation (Cat. No. 03CH37422), Vol. 2, IEEE, 2003, pp. 1620–1626.

[14] M. Vukobratović, B. Borovac, Zero-moment point—thirty five years of its life, International journal of humanoid robotics 1 (01) (2004) 157–173.

[15] J. Liu, H. Chen, P. M. Wensing, W. Zhang, Instantaneous capture input for balancing the variable height inverted pendulum, IEEE Robotics and Automation Letters 6 (4) (2021) 7421–7428.

[16] K. Van Heerden, Real-time variable center of mass height trajectory planning for humanoids robots, IEEE Robotics and Automation Letters 2 (1) (2016) 135–142.

[17] B. Kaddar, Y. Aoustin, C. Chevallereau, Arm swing effects on walking bipedal gaits composed of impact, single and double support phases, Robotics and Autonomous Systems 66 (2015) 104–115.

[18] F. Iida, Y. Minekawa, J. Rummel, A. Seyfarth, Toward a human-like biped robot with compliant legs, Robotics and Autonomous Systems 57 (2) (2009) 139–144.

[19] H. Sun, J. Yang, Y. Jia, C. Wang, Posture control of legged locomotion based on virtual pivot point concept, Journal of Bionic Engineering 20 (6) (2023) 2683–2702.

[20] M. A. Sharbafi, A. Seyfarth, Fmch: A new model for human-like postural control in walking, in: 2015 IEEE/RSJ International Conference on Intelligent Robots and Systems (IROS), IEEE, 2015, pp. 5742–5747.

[21] J. Pratt, J. Carff, S. Drakunov, A. Goswami, Capture point: A step toward humanoid push recovery, in: 2006 6th IEEE-RAS international conference on humanoid robots, IEEE, 2006, pp. 200–207.

[22] S. Caron, A. Escande, L. Lanari, B. Mallein, Capturability-based pattern generation for walking with variable height, IEEE Transactions on Robotics 36 (2) (2019) 517–536.

[23] K. Guan, K. Yamamoto, Y. Nakamura, Virtual-mass-ellipsoid inverted pendulum model and its applications to 3d bipedal locomotion on uneven terrains, in: 2019 IEEE/RSJ International Conference on Intelligent Robots and Systems (IROS), IEEE, 2019, pp. 1401–1406.

[24] J. Ding, C. Zhou, S. Xin, X. Xiao, N. G. Tsagarakis, Nonlinear model predictive control for robust bipedal locomotion: exploring angular momentum and com height changes, Advanced Robotics 35 (18) (2021) 1079–1097.

[25] J. Reher, A. D. Ames, Dynamic walking: Toward agile and efficient bipedal robots, Annual Review of Control, Robotics, and Autonomous Systems 4 (2021) 535–572.

[26] W. Zijlstra, A. L. Hof, Displacement of the pelvis during human walking: experimental data and model predictions, Gait & posture 6 (3) (1997) 249–262.

[27] T. Otani, K. Hashimoto, S. Miyamae, H. Ueta, A. Natsuhara, M. Sakaguchi, Y. Kawakami, H.-O. Lim, A. Takanishi, Upper-body control and mechanism of humanoids to compensate for angular momentum in the yaw direction based on human running, Applied Sciences 8 (1) (2018) 44.

[28] G. H. Negri, L. K. Rosa, M. S. Cavalca, L. A. Celiberto Jr, E. B. de Figueiredo, Nonlinear predictive control applied to a biped walker with adjustable step length using a passive walking-based reference generator, Optimal Control Applications and Methods 41 (3) (2020) 729–747.

[29] A. D. Kuo, Stabilization of lateral motion in passive dynamic walking, The International Journal of Robotics Research 18 (9) (1999) 917–930.

[30] J. Ding, X. Xiao, Y. Wang, Preview control with adaptive fuzzy strategy for online biped gait generation and walking control, International Journal of Robotics & Automation 31 (6) (2016) 677–699.

[31] B. Park, J. Park, Heel-strike and toe-off walking of humanoid robot using quadratic programming considering the foot contact states, Robotics and Autonomous Systems 163 (2023) 104396.

[32] W. Z. Peng, C. Mummolo, H. Song, J. H. Kim, Whole-body balance stability regions for multi-level momentum and stepping strategies, Mechanism and Machine Theory 174 (2022) 104880.

[33] Z. Sun, B. Zhang, Y. Sun, Z. Pang, C. Cheng, A novel superlinearly convergent trust region-sequential quadratic programming approach for optimal gait of bipedal robots via nonlinear model predictive control, Journal of Intelligent & Robotic Systems 100 (2) (2020) 401–416.

[34] J. Ueda, K. Shirase, Y. Matsumoto, S. Oda, T. Ogasawa, Momentum compensation for fast dynamic walking of humanoids based on pelvic rotation of contact sport athletes, in: Humanoid Robots, 2004 4th IEEE/RAS International Conference on, IEEE, 2005, pp. 592–597.

[35] T. Hirabayashi, B. Ugurlu, A. Kawamura, C. Zhu, Yaw moment compensation of biped fast walking using 3d inverted pendulum, in: IEEE International Workshop on Advanced Motion Control, IEEE, 2008, pp. 296–230.

[36] Y. Liang, C. Deng, Yaw moment compensation for humanoid robot via arms swinging, The Open Automation and Control Systems Journal 6 (1) (2014) 1371–1377.

[37] R. Cisneros, M. Benallegue, M. Morisawa, E. Yoshida, F. Kanehiro, Partial yaw moment compensation using an optimization-based multi-objective motion solver, in: 2018 IEEE-RAS 18th International Conference on Humanoid Robots (Humanoids), IEEE, 2018, pp. 1017–1024.

[38] A. Miyata, S. Miyahara, D. N. Nenchev, Walking with arm swinging and pelvis rotation generated with the relative angular acceleration, IEEE Robotics and Automation Letters 5 (1) (2019) 151–158.

[39] B. Ugurlu, J. A. Saglia, N. G. Tsagarakis, D. G. Caldwell, Yaw moment compensation for bipedal robots via intrinsic angular momentum constraint, International Journal of Humanoid Robotics 9 (04) (2012) 1250033.

[40] D. N. Nenchev, R. Iizuka, Emergent humanoid robot motion synergies derived from the momentum equilibrium principle and the distribution of momentum, IEEE Transactions on Robotics 38 (1) (2021) 536–555.

[41] T.-Y. Chen, S. Shigaki, K. Hosoda, Bevel-geared mechanical foot: a bioinspired robotic foot compensating yaw moment of bipedal walking, Advanced Robotics 36 (13) (2022) 631–640.

[42] C. Zhu, A. Kawamura, What is the real frictional constraint in biped walking? - discussion on frictional slip with rotation, in: 2006 IEEE/RSJ International Conference on Intelligent Robots and Systems, IROS 2006, October 9-15, 2006, Beijing, China, IEEE, 2006, pp. 5762–5768.

[43] S. Huang, Z. Wei, Z. Duan, C. Sun, Y. Wang, Y. Tao, Y. Zhang, Y. Kan, E. Meyer, D. Li, et al., Reexamination of damping in sliding friction, Physical Review Letters 132 (5) (2024) 056203.

[44] J. Jian, P. Liu, J. Yin, C. Zhang, M. Chao, A qcqp-based splitting sqp algorithm for two-block nonconvex constrained optimization problems with application, Journal of Computational and Applied Mathematics 390 (2021) 113368.

[45] L. Tesio, V. Rota, The motion of body center of mass during walking: a review oriented to clinical applications, Frontiers in neurology 10 (2019) 999.

[46] A. E. Minetti, C. Cisotti, O. S. Mian, The mathematical description of the body centre of mass 3d path in human and animal locomotion, Journal of biomechanics 44 (8) (2011) 1471–1477.

[47] S. Bertrand, O. Bruneau, F. Ouezdou, S. Alfayad, Closed-form solutions of inverse kinematic models for the control of a biped robot with 8 active degrees of freedom per leg, Mechanism and Machine Theory 49 (2012) 117–140.

[48] Z. Xie, L. Li, X. Luo, A foot-ground interaction model based on contact stability optimization for legged robot, Journal of Mechanical Science and Technology 36 (2) (2022) 921–932.

[49] C.-C. Wu, V. Zordan, Goal-directed stepping with momentum control, in: Proceedings of the 2010 ACM SIGGRAPH/Eurographics symposium on Computer animation, 2010, pp. 113–118.

[50] Z. Xie, L. Li, X. Luo, Human-like strategies exploiting momentum for biped robot balance recovery, Iranian Journal of Science and Technology, Transactions of Mechanical Engineering 46 (3) (2022) 599–615.

[51] Z. Xie, L. Li, X. Luo, Optimization of the ground reaction force for the humanoid robot balance control, Acta Mechanica 232 (10) (2021) 4151–4167.

[52] B. Siciliano, O. Khatib, Springer Handbook of Robotics, Springer, 2016.
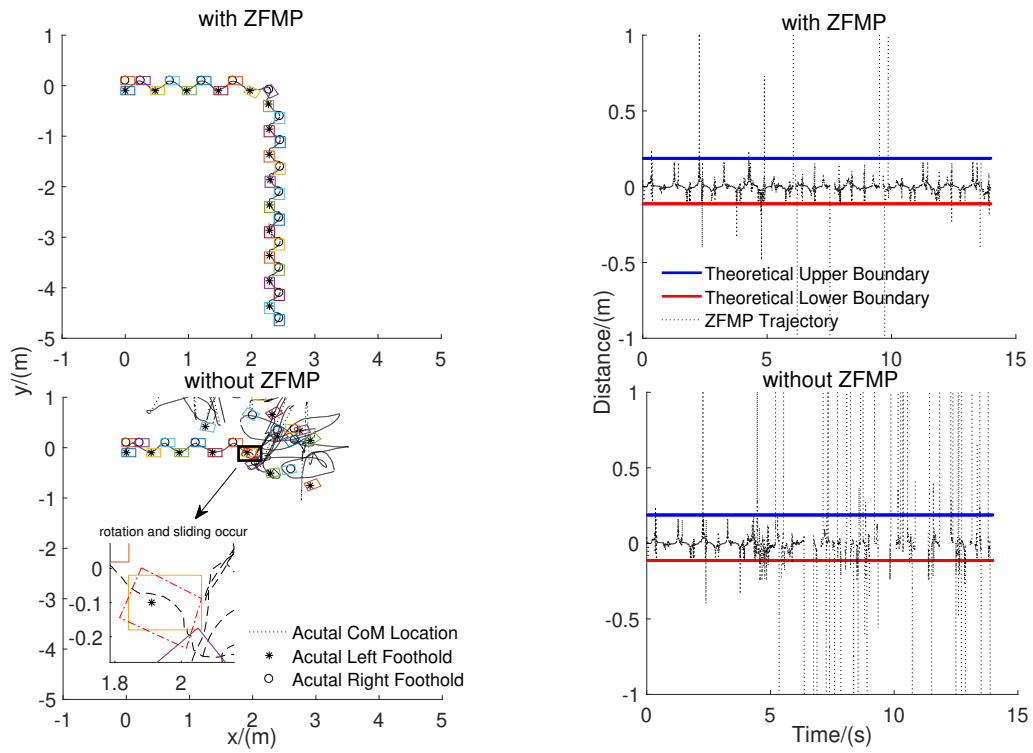
(a) The footholds and CoM trajectory in the horizontal plane with (top) and without (bottom) ZFMP

(b) ZFMP during the walking with (top) and without (bottom) ZFMP
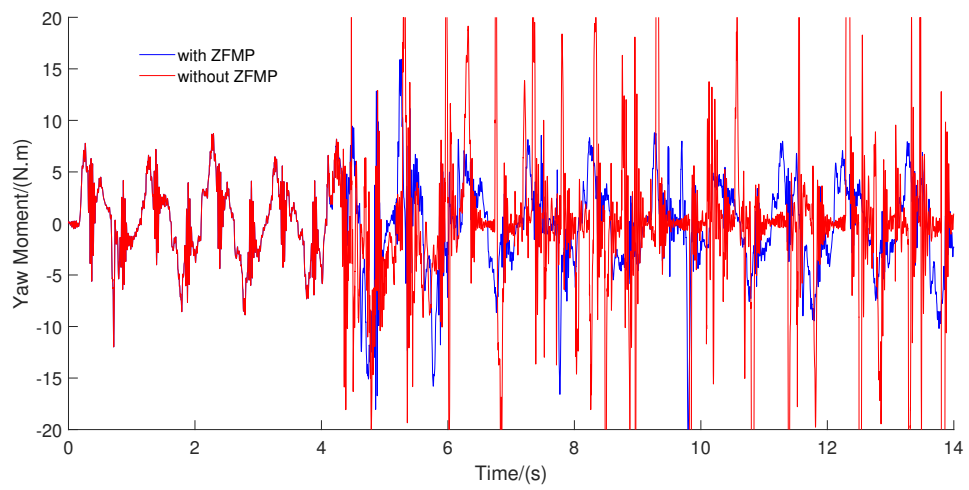
(c) Yaw moment during steering

Figure 10: The results of the robot steers with and without ZFMP constraint.
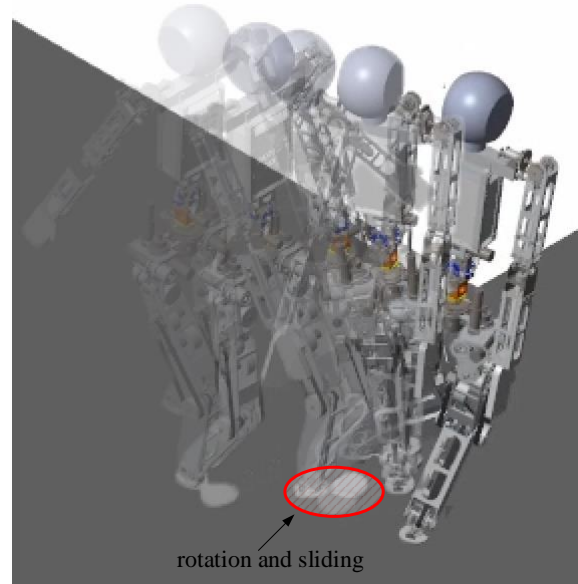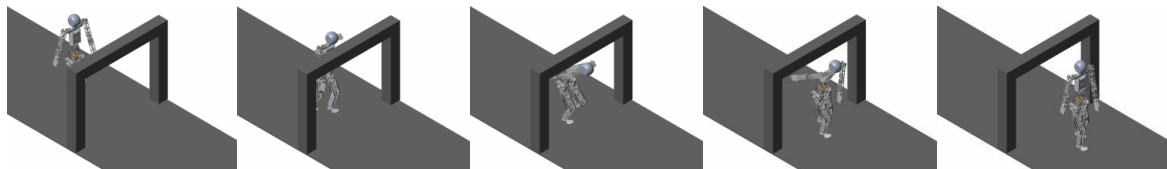
Figure 11: The moment the rotation and sliding occur.

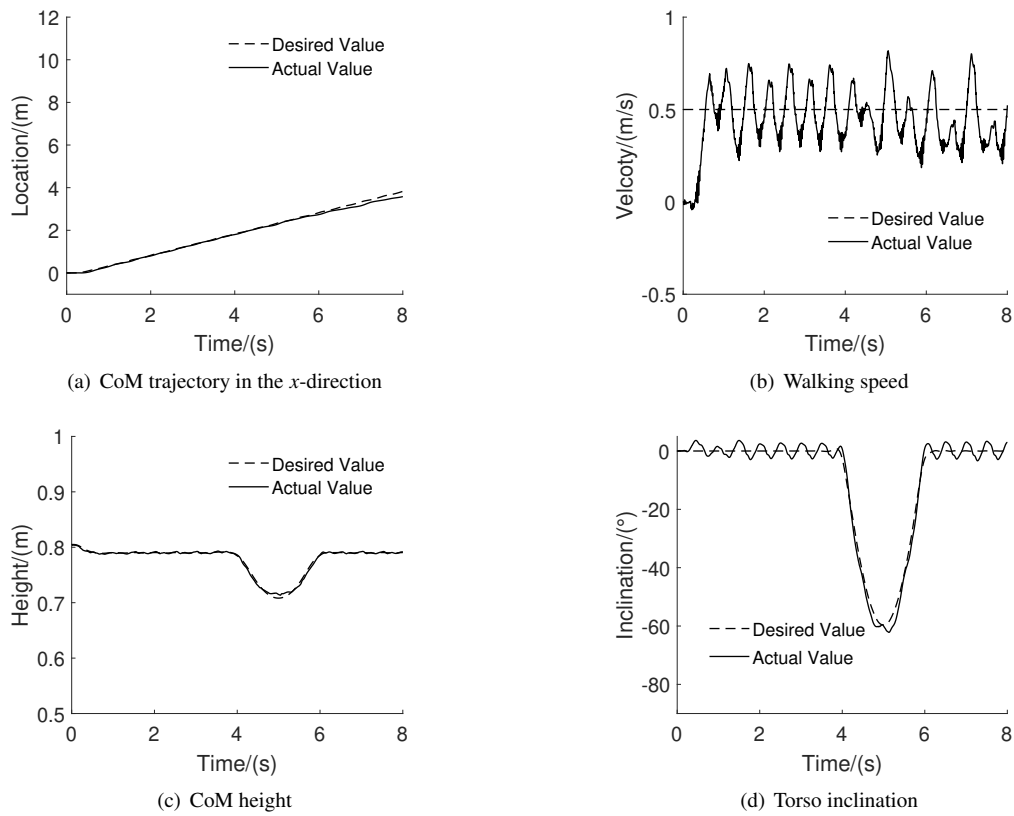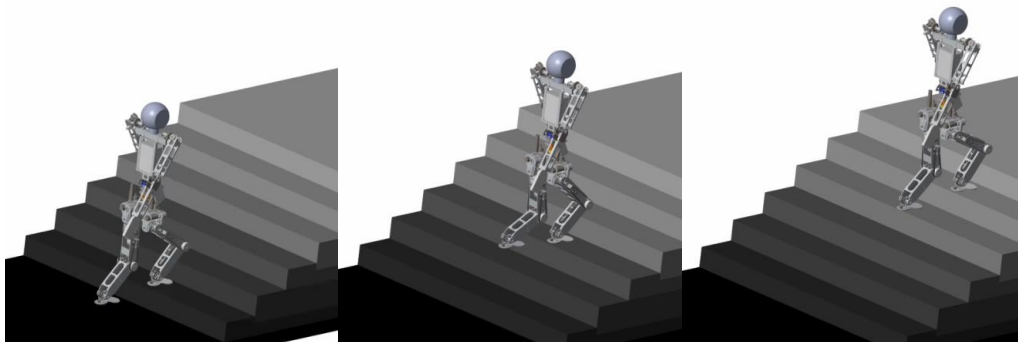Figure 12: The snapshots of the robot passing a low door.

(a) CoM trajectory in the x-direction

(b) Walking speed

(c) CoM height

(d) Torso inclination

Figure 13: The motion of passing a low door
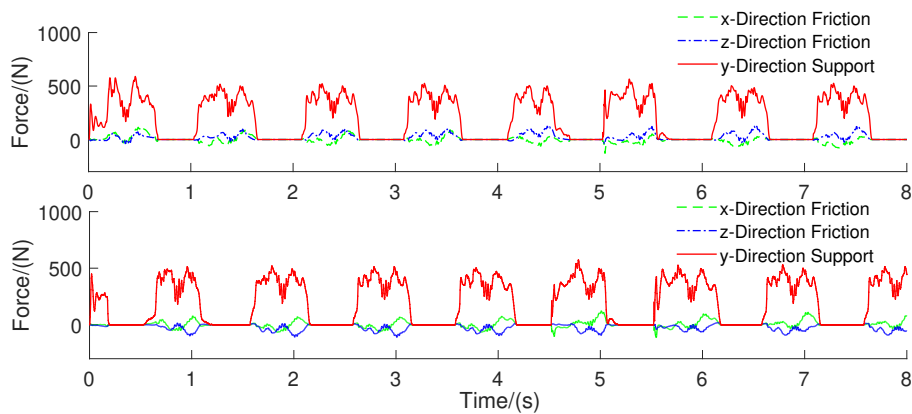
Figure 14: GRFs during walking while passing a low door.
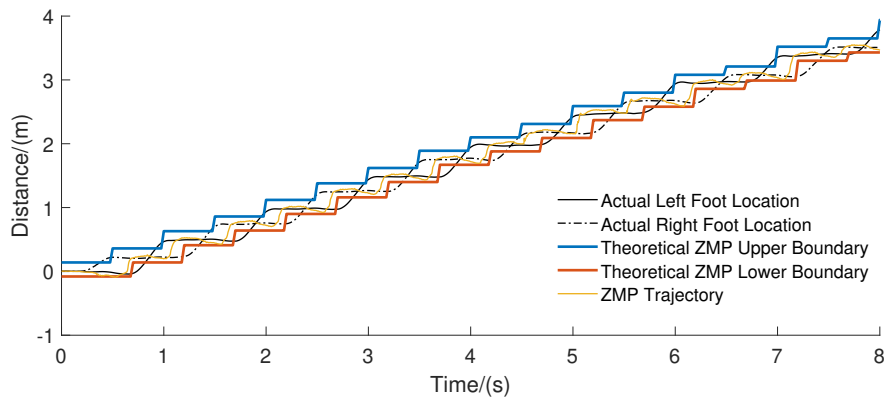
Figure 15: The actual feet and ZMP trajectories while passing a low door.
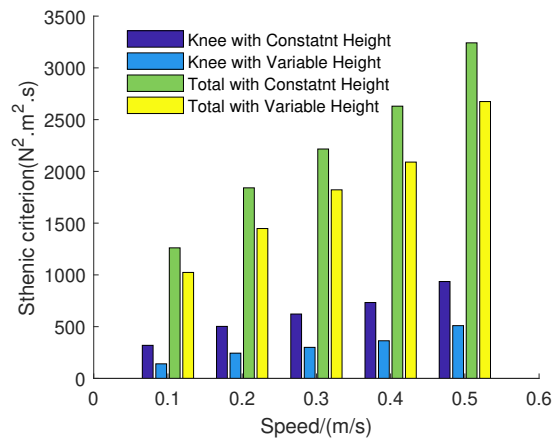
Figure 16: The one-step energy consumption of the robot with different walking speed.
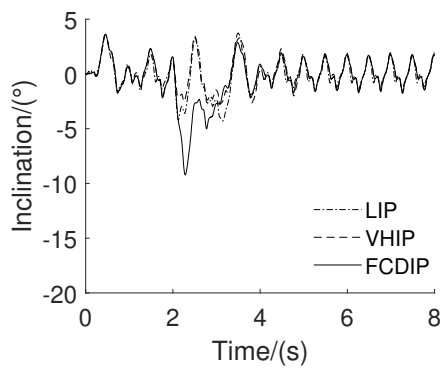

Figure 17: The snapshots of the robot going upstairs.

25
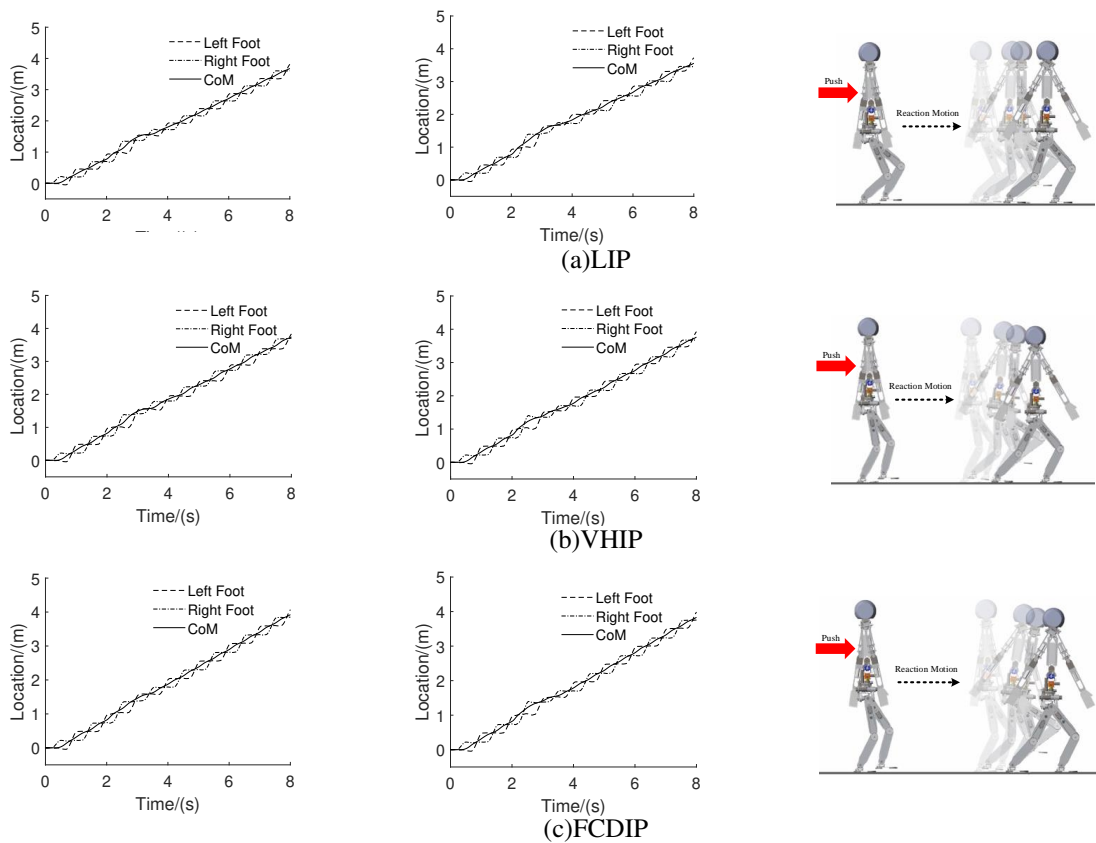
Figure 18: Reaction step of robot under the forward pushes. In each row, the first two columns represent trajectories of feet and CoM in the presence of external forces of 150N and 250N, respectively. The last column denotes a snapshot of the robot's reactive motion under the push with the magnitude of 250N.
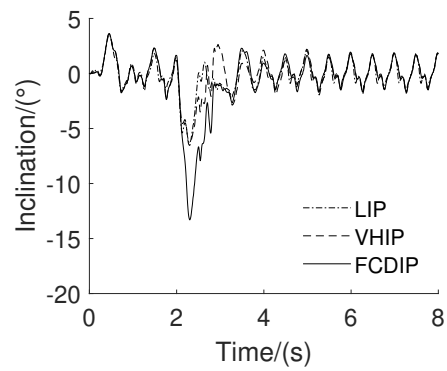
(a) Inclination angle of torso under push with the magnitude of 150N. (b) Inclination angle of torso under push with the magnitude of 250N.
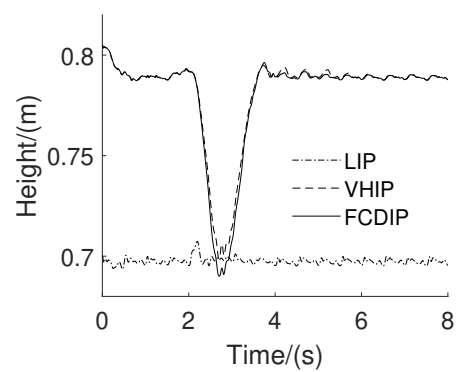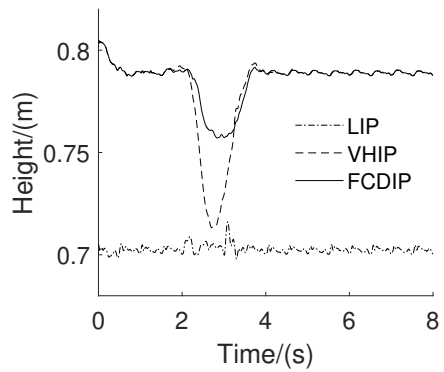
(c) CoM height under push with the magnitude of 150N.

(d) CoM height under push with the magnitude of 250N.

Figure 19: The results of push recovery.

27